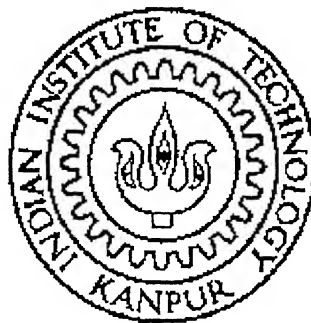


**ULTRASONIC TOMOGRAPHIC RECONSTRUCTION OF
DEFECTS IN 2-DIMENSIONS WITH RAY BENDING
CONSIDERATION**

A Thesis Submitted
in Partial Fulfillment of the Requirements
for the Degree of
MASTER OF TECHNOLOGY

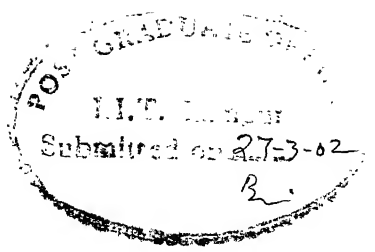
by
PRADIPTA RANJAN BASU-MANDAL



to the
DEPARTMENT OF MECHANICAL ENGINEERING
INDIAN INSTITUTE OF TECHNOLOGY KANPUR

March, 2002

CERTIFICATE



It is certified that the work contained in the thesis entitled **Ultrasonic Tomographic Reconstruction of Defects in 2-Dimensions with Ray Bending Consideration** by Pradipta Ranjan Basu-Mandal has been carried out under my supervision and it has not been submitted elsewhere for a degree.

N N Kishore

Dr. N.N.Kishore

(Professor and Head)

Department of Mechanical Engineering

Indian Institute of Technology, Kanpur

March, 2002

29 APR 2002

पुस्तकालय
भारतीय प्रौद्योगिकी संशोधन कानपुर
वर्षाप्ति क्र० A.....139537-



ACKNOWLEDGEMENTS

I wish to express my profound gratitude and indebtedness towards my thesis supervisor Dr. N.N. Kishore for his inspiring guidance and constant encouragement.

I am especially thankful to my colleague, Mr. Nitesh Jain for providing me with the time of flight data which I used in my thesis work.

I extend my thanks to other colleagues in my laboratory, Dr. A.K.Agrawal, Mr. S.K. Rathore, Mr. G.Daliraju, Sqn Ldr P.S.Sarin, Mr.S.K.Sahoo, Mr. Samuel Jeevanand, Mr. S.B. Kumar and Mr. S.Trivedi for their constant encouragement.

I would also like to thank all my friends, Shamik, Shamikc, Omprakash, Arijit, Abir, Arnab, Debadi, Suman and Tathagata with whom I had good company during my stay at Hall-5. I will cherish the moments spent together with them forever.

I wish to record my sense of gratitude towards my parents, uncle and aunt, my elder sister and to my cousin brothers without whose support and encouragement this work would have remained unfinished.

Indian Institute of Technology, Kanpur.
March 2002.

Pradipta Ranjan Basu-Mandal

Abstract

In ultrasonic non-destructive testing and evaluation, the different features of ultrasonic waves, namely frequency, amplitude, time of flight etc can be used for detection and sizing of internal defects. Ultrasonic Tomography is used to characterize a defect or inhomogeneity by time of flight information. The accuracy of reconstruction depends on the accuracy of time of flight estimation. The present work is concerned with tomographic reconstruction of square, circular and elliptical defects using simulated time of flight data. Three combinations of base material and insert material, namely, (1) Steel with Aluminum insert, (2) Steel with Nickel insert and (3) Steel with Brass insert have been taken in this present work to study the quality of reconstruction with the relative variation in longitudinal sonic velocity between the base and the insert material. Snell's law has been used to ascertain the path taken up by the ultrasonic ray in the presence of a refraction artifact. Standard edge detection techniques have been applied to find out the interface for refraction in the presence of a curved defect. From the nature of the reconstructed images the optimum range for the relaxation parameter has been identified within which there is a good balance between the quality of reconstruction and also the computer run time. All the reconstructions have been obtained using Mayinger ART algorithm. The effect of relaxation parameter on the rate of convergence of the iterative algorithm has also been studied. Tables providing values of normalized RMS errors have been given for all the combinations of the base and insert materials and for all defect geometries. The reconstructed images obtained using curved ray approach have been compared with the same obtained using straight ray assumption. Another table furnishing the values of the normalized RMS errors in the case of straight ray approach has been given. Finally, a table showing a comparison of the times taken to execute the code using curved ray approach and without using curved ray approach has been provided.

**DEDICATED
TO
MY PARENTS**

CONTENTS

1. Introduction	
1.1 Introduction	1
1.2 Literature survey	3
1.3 Present work	5
1.4 Thesis organisation	5
2. Reconstruction methods and problem formulation	7
2.1 Introduction	7
2.2 Reconstruction methods	7
2.2.1 Algebraic reconstruction techniques	9
2.3 Computer implementation of the procedure	13
2.4 Formulation of the present problem in the light of algebraic reconstruction algorithm	16
2.5 Closure	17
3. Ray bending and edge detection	18
3.1 Introduction	18
3.2 Ultrasonic wave propagation	18
3.3 Reflection and transmission at an interface	20
3.4 Ultrasonic ray theory	21
3.5 Image analysis and edge detection	22
3.5.1 Point detection	22
3.5.2 Line detection	23
3.5.3 Edge detection	24
3.5.4 Threshold selection	28
3.5.5 Second order derivative edge detection	28
3.6 Closure	29
4. Results and discussions	30
4.1 Introduction	30
4.2 Details of test cases	31
4.3 Image reconstruction	34
4.3.1 Images obtained without ray bending consideration	35
4.3.2 Images obtained with ray bending consideration	35
4.4 Slowness values	36
4.5 RMS error	37
4.6 Closure	60
5. Conclusions and scope for future work	61
5.1 Conclusions	61
5.2 Scope for future work	62

List of Figures

2.1 Intercept made by the i^{th} ray in the j^{th} pixel	9
3.1 Reflection and refraction at a solid-solid interface	21
4.1 Grid for discretizing the domain	31
4.2 Intercept made by the i^{th} ray in the j^{th} pixel	32
4.3 Three fan beams at 90° for circular Aluminium insert	44
4.4 Three fan beams at 0° for circular Nickel insert	44
4.5 Three fan beams at 45° for circular Brass insert	45
4.6 Total ray-path for circular Aluminium insert	45
4.7 Total ray-path for circular Nickel insert	46
4.8-4.9 Graphs of RMS errors vs Number of iterations	47
4.10-4.12 Images obtained without ray bending for Brass insert	48
4.13-4.16 Images obtained with ray bending for square Aluminium insert	49
4.17-4.20 Images obtained with ray bending for circular Aluminium insert	50
4.21-4.24 Images obtained with ray bending for elliptical Aluminium insert	51
4.25-4.27 Contour plots for three different defect geometries	52
4.28-4.31 Images obtained with ray bending for square Nickel insert	54
4.32-4.35 Images obtained with ray bending for circular Nickel insert	55
4.36-4.39 Images obtained with ray bending for elliptical Nickel insert	56
4.40-4.43 Images obtained with ray bending for square Brass insert	57
4.44-4.47 Images obtained with ray bending for circular Brass insert	58
4.48-4.51 Images obtained with ray bending for elliptical Brass insert	59

List of Tables

4.1 Properties of base and insert materials	31
4.2 Normalized RMS errors for square Aluminium insert	37
4.3 Normalized RMS errors for circular Aluminium insert	38
4.4 Normalized RMS errors for elliptical Aluminium insert	38
4.5 Normalized RMS errors for square Nickel insert	39
4.6 Normalized RMS errors for circular Nickel insert	39
4.7 Normalized RMS errors for elliptical Nickel insert	40
4.8 Normalized RMS errors for square Brass insert	40
4.9 Normalized RMS errors for circular Brass insert	41
4.10 Normalized RMS errors for elliptical Brass insert	41
4.11 Normalized RMS errors for circular Brass insert without ray bending	42
4.12 Normalized RMS errors for elliptical Brass insert	43
4.13 Comparison of runtime with and without ray bending	43

List of symbols

τ Time of flight

s^k Slowness in the k^{th} pixel

w_{ij} Weight (length of intercept) made by the i^{th} ray in the j^{th} pixel

λ Relaxation parameter

Chapter 1

Introduction

1.1 Introduction

Non-destructive testing and evaluation methods play a pivotal role in quality assurance of structural members during their manufacturing stage and later during their operational period. Being one of the most commonly used non-destructive testing methods, ultrasonic testing is rapidly developing in the recent years. This method uses ultrasonic waves for detection and sizing of internal flaws present in materials. In this method, piezo-electric transducer (probe) generates ultrasonic waves, which propagate in the elastic medium and are detected either by the same or by a different transducer.

In general, the transit time of the acoustic echo wave is used to measure the distance of a flaw or insertion from the probe and the amplitude of the reflected wave is used to size the flaw. In the pulse-echo technique, a single probe is used to transmit and receive the signal. Another technique, called through transmission technique, employs two separate transducers (a transmitter and a receiver) to transmit and receive the wave. This technique requires access to both sides of the specimen, as the probes are placed on opposite sides of the specimen.

Ultrasonic signals can be displayed in A-scan, B-scan or C-scan formats. An A-scan indicates a variation of the signal amplitude with time at a point. The familiar screen image is an A-scan presentation, which furnishes one-dimensional description of a given test point. In the case of B-scan, the displayed signal is the trace of time versus linear

position. In the case of two-dimensional scanning of a test-piece, the results can be represented by means of a C-scan. This furnishes a top-view of the scanned surface. C-scan systems are especially computer-controlled. Ultrasonic systems displaying both B-scan and C-scan formats are also called P-scan systems.

Tomography is a procedure where internal body images at a predetermined plane are recorded by means of the tomograph, a computer-driven machine that builds the image from multiple x-ray measurements. It is also called body section roentgenography. It can produce sophisticated cross-sectional or three-dimensional pictures of the internal organs, which can be used to identify abnormalities, for example, tumors. There are numerous applications for reconstructing images from their projections. The spatial resolution and tissue discrimination capabilities of this technique far surpass what could be achieved with conventional x-ray imaging. Image reconstruction from projections is also used in nuclear medicine to map the distribution of the concentration of gamma-ray emitting radionuclides in a given cross section of the human body. Another medical application area is computed tomographic imaging with ultrasound. Due to the radiation hazards associated with x-rays, ultrasonic imaging is gaining considerable attention. Non-medical applications in which images can be reconstructed from projections include radioastronomy, optical interferometry, electron microscopy and geophysical exploration.

In contrast with X-rays, tomographic imaging with ultrasound is made difficult due to the fact that the rays of sound energy do not necessarily travel in a rectilinear fashion when an interface is encountered. This phenomenon of refraction while using ultrasound as a source has posed major challenges in the field of tomographic reconstruction. To account for refraction, the acoustic analogue of Snell's law is widely used.

This study is concerned with tomographic reconstruction of isotropic specimens with artificially implanted defects. For the above-mentioned reconstruction, the propagation characteristics (speed or amplitude) of the acoustic wave are measured. These propagation characteristics, namely, speed and amplitude are directly related to the material property of interest. Therefore, the properties, which can be measured experimentally, can often be approximated as line integrals along the path of the

propagating disturbance. For acoustic experiments in isotropic media, one possible formulation of the problem is in terms of transit time between the source and the receiver.

1.2 Literature Survey

Theoretical studies on the elastic wave propagation found in literature are manifold, most of which deal with isotropic media, only a few are concerned with wave propagation in anisotropic media. Extending the scope of interest to the wave scattering problem in anisotropic materials for the purpose of location and classification of defects and other inhomogeneities, respective studies are approximate in character and mostly confined to particular geometries and material symmetry. Chen [1] first presented a coordinate free approach, which is useful in dealing with lay structures.

Synge [2] developed the theory of slowness surfaces. After that Musgrave [3] introduced the idea of superimposing the slowness surface on the geometric space, which contains the incident and emerging waves.

Previously, modelling techniques for inhomogeneous materials have been developed with emphasis on inspection on austenitic welds and claddings. Although the numerical methods such as finite difference, finite element or finite integration provide good results, they suffer from the inherent requirement of large computation times and hardware requirements.

Leander [4] developed the relation between the wavefront speed, which is the speed of propagation of a front of a pulse. Crandell's [5] work was based on the use of slowness surfaces to represent wave reflections.

Very few quantitative results have been published on the reflection and refraction of plane elastic waves from an interface in a general anisotropic media. Musgrave and Fedorov [6] summarized the general theoretical results for the reflection-refraction problems in their comprehensive books. Auld [7] discussed several examples for planes of symmetry. Henneke [8] and McNiven et al [9] reviewed Fedorov's method and discussed critical angle phenomena for the elastic waves at an interface. These works mainly focussed on finding reflection and refraction angles using geometrical plotting on slowness surfaces.

More recently, Rokhlin et al [10] have described a unified approach to the numerical solution of the reflection-refraction problem for generally anisotropic media.

Harker et al [11] presented a full numerical solution of the wave equation and showed that ray tracing method gives similar and consistent results.

Kak [12] reviewed developments in Ultrasonic Computerized Tomography and has presented the reconstruction of velocity and attenuation coefficient images in medical applications. The effects of refraction were ignored as only soft tissue-structures were studied. Digital ray-tracing algorithms have been developed by many workers to account for refraction in ultrasound tomography. They have used Snell's law, Fermat's principle and the Eikonal equation in geometrical optics for it. Kak and Andersen [13] have presented a review of digital ray tracing in two-dimensional refractive index field. The various aspects of numerical implementation like discretization, numerical interpolation schemes, step-size and the use of smoothing windows have been dealt comprehensively in the above-mentioned work.

Bold et al [14] have compared the different integration methods with regard to the three algorithms reported by Kak and Andersen. They have found that fourth order methods give a good combination of accuracy along with simplicity and speed. Evidently, accuracy increases with the increase in the order of integration and with the decrease in step-size.

Wang et al [15] have developed a technique for ray tracing in non-homogeneous media (both isotropic and anisotropic). Their approach is based upon Fermat's principle and can be readily incorporated into tomographic reconstruction algorithms. They have also investigated the effect of ray-bending on the accuracy of acoustic tomograms.

Denis et al [16] have shown that the reconstruction quality can be improved significantly for refractive index variations of upto 10% using curved-ray methods. They have presented both simulation and experimental results to verify the reduction of refraction artifacts by this method.

Rathore et al [17] have carried out the tomographic reconstruction of an object containing two defect geometries at a fixed distance. In their work, the contrast i.e. the relative difference in material velocity or refractive index between the defect and base material, is varied to study the reconstruction of two defects separately. In a later work,

Rathore et al [18] have varied the distance between two defect geometries so as to establish the minimum gap at which they can be resolved.

1.3 Present Work

In the present work, the tomographic reconstruction of square, circular and elliptical defects in isotropic materials, using simulated time of flight data has been carried out. The quality of the reconstruction has been studied by varying the contrast, i.e. the relative difference in material velocity or refractive index between the defect and the base material. In the present work, several rays are considered from a single source and the one, which reaches nearest to the receiver, has been considered. The materials selected for the purpose of investigation are (1) Steel with Aluminium insert, (2) Steel with Nickel insert and (3) Steel with brass insert. Snell's law has been used to account for the bending of the ultrasonic wave inside the medium. Edge detection has been applied to find out the orientation of the interface for refraction in the presence of a curved artifact. The relaxation parameter has also been varied to study its influence on the convergence rate of the iterative algorithm. Plots indicating the paths taken up by the ultrasonic rays after several iterations and tables furnishing the values of the normalized RMS errors for different values of the relaxation parameter have also been provided in the work.

1.4 Thesis organization

The various chapters in the thesis deal with the following aspects.

- Chapter 2 presents the problem formulation in some detail, the tomographic algorithms that have been used for the reconstruction, the other tomographic algorithms that are in vogue and finally a discussion on the computer implementation of these algorithms.
- Chapter 3 deals with the effect of ray bending caused by the presence of refraction artifacts. A somewhat comprehensive discussion on edge detection used here to find out the orientation of the interface for refraction in the presence of a curved artifact has also been incorporated in this chapter.
- Chapter 4 gives the reconstructed slowness images for the three discussed combinations of the parent material and the insert material. It also discusses the effect

of relaxation parameter on the convergence rate of the tomographic algorithm used in this work. Tables supplying normalized RMS errors for different values of the relaxation parameter and plots showing typical ray-paths after several iterations have been provided along with this chapter.

- Chapter 5 finally concludes the present work and gives suggestions for future work.

Chapter 2

Reconstruction Methods and Problem Formulation

2.1 Introduction

The applications of computerized tomography (CT) in today's engineering world are manifold. It has got immense applications in the field of medicine as well. In conventional projection radiography, the result is obtained in the form of a shadowgraph requiring a good interpretation. CT, however, uses tomographic reconstruction to combine information from multiple projections. Thus, the CT information is displayed quantitatively as a reconstructed slice plane of the object and it can provide accurate quantitative measures of material characteristics in a small volume of the component.

Although computerized tomography was originally conceived for X-rays, in recent times, its horizon has considerably broadened with its successful implementation for other energy sources such as ultrasonics, lasers and magnetic resonance etc. Among these, ultrasonic tomography has special applications in the field of non-destructive evaluation. Ultrasonic tomography can be defined as a technique to determine values of a spatially varying acoustic parameter of interest across a slice through an object.

2.2 Reconstruction methods

Tomography can be classified into (a) transform (b) series expansion and (c) optimization methods. Transform methods generally require a large number of projections for a meaningful answer. However, in most of the cases it is not practicable to record such a

large number of projections partly owing to inconvenience and partly due to time and cost. Hence, as a rule requirement of a large number of projections is not desirable and one must look for methods that converge within a few iterations. Limited-view tomography is best accomplished using the series-expansion method. As limited data tomography does not have a unique solution, the algorithms are expected to be sensitive to the initial guess of the field that start the iterations. Optimization-based algorithms are known to be independent of initial guess, but the choice of the optimization function plays an important role in the result obtained. Depending on the mathematical definition used, the entropy extremization route may yield good results, while the entropy minimization principle may be suitable in other applications. For the algebraic techniques considered in the present study, an unbiased initial guess such as a constant profile was seen to be good enough to predict the correct field variable. Tomography, being an inverse technique was seen to preserve the noise in the initial data. However, the dominant trend in the field variable was captured during tomographic inversion. Actually the problem of reconstruction is a problem of inversion of a rectangular matrix. Iterative techniques that are used in tomography can be viewed as developing a generalized inverse of the matrix. However, the matrices are mainly sparse ones. Thus general purpose matrix libraries can not be used to invert them since they are highly ill-conditioned and rectangular in structure. The tomographic algorithms can be seen as a systematic route towards a meaningful inversion of the matrix.

Series expansion methods have been adopted as the appropriate technique for image reconstruction. These methods are iterative in nature and consist necessarily of four major steps, namely:

1. Initial assumption of the field to be reconstructed
2. Calculation of the correction
3. Application of the correction
4. Test for convergence

2.2.1 Algebraic reconstruction techniques

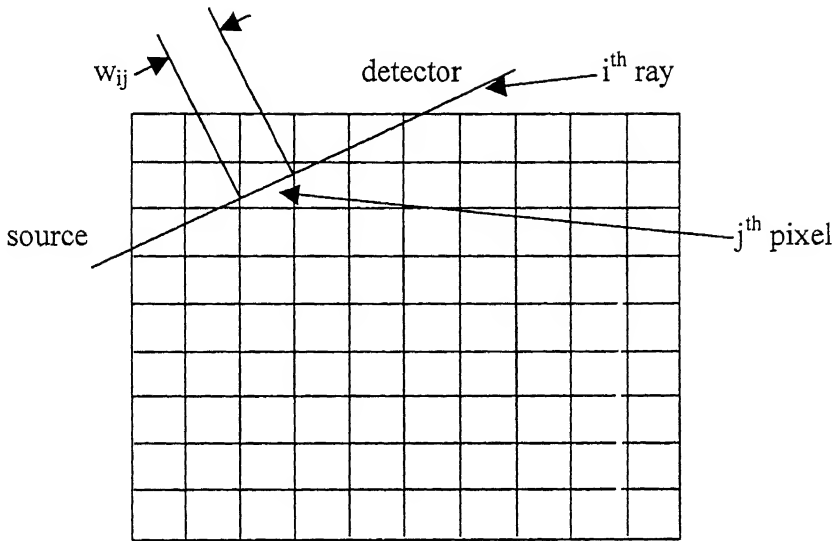


Figure 2.1, Intercept made by the i^{th} ray in the j^{th} pixel

In Figure 2.1 a square grid on the image $g(x,y)$ has been superimposed with the premise that in each element of the grid $g(x,y)$ is constant. The field value in the m^{th} cell is denoted by x_m . The total number of cells is taken to be N . In algebraic reconstruction techniques a ray is defined somewhat differently. In this context, a ray is now defined as a “fat” line running through the xy plane. The other important assumption behind the theory of algebraic reconstruction techniques is that the ray-width is approximately equal to the image cell width. In case of defect reconstruction for non-destructive evaluation purposes, the projections are basically the time-of-flight data i.e. the transit time between the source and the receiver. The relationship connecting the field value (x_i) with the projection value (p_i) can be expressed as

$$\sum_{j=1}^N W_{ij} x_j = p_i, i = 1, 2, \dots, M \quad (2.1)$$

where “ M ” is the total number of rays (in all projections), and W_{ij} is the weighting factor that represents the contribution of the j^{th} cell to the i^{th} ray integral. Also “ N ” is the total number of cells in the grid.

Conventional matrix methods can be used to invert the system of equations in Eq.(2.1) for small values of “M” and “N”. However, in practice the values of “N” are quite large, sometimes of the order of 65,000 (for 256x256 images), and in most cases for images of the above-mentioned size, “M” also has the same magnitude. Thus the weight matrix becomes too large, which precludes any possibility of direct matrix inversion. Also the weight matrix is a sparse one with many of its elements being zero. General-purpose matrix libraries cannot be used to invert such matrices since they are highly ill-conditioned and rectangular in structure. Of course, when noise is present in the measurement data and when M<N, even for small N, it is not possible to use direct matrix inversion, and some least-squares methods may have to be used. But such methods are impractical for large values of both M and N.

For large values of M and N, there exist very attractive iterative methods for solving the system of equations given in Eq. (2.1). The earliest methods were proposed by Kacmarz [19], which is commonly referred to, as the method of projections. Writing Eq. (2.1) in an expanded form, the computational steps involved in the method are explained.

$$W_{11}x_1 + W_{12}x_2 + W_{13}x_3 + \dots + W_{1N}x_N = p_1 \quad (2.2)$$

$$W_{21}x_1 + W_{22}x_2 + W_{23}x_3 + \dots + W_{2N}x_N = p_2 \quad (2.3)$$

.....

.....

$$W_{M1}x_1 + W_{M2}x_2 + W_{M3}x_3 + \dots + W_{MN}x_N = p_M \quad (2.4)$$

A grid representation with N cells gives an image N degrees of freedom. Thus, an image which is represented as (x_1, x_2, \dots, x_N) may be considered as a single point in an N-dimensional space. In this space each of the above equations represents a hyperplane. When a unique solution to this system of equations exists, the intersection of all these hyperplanes is a single point giving the solution. In this context for the purpose of explanation the case of two variables is considered.

They satisfy the following equations:

$$W_{11}x_1 + W_{12}x_2 = p_1 \quad (2.5)$$

$$W_{21}x_1 + W_{22}x_2 = p_2 \quad (2.6)$$

The computational procedure for locating the solution to the system of equations consists of starting with an initial guess, projecting this initial guess onto the first line, reprojecting the resultant point on the second line and then projecting back onto the first line, and so on until the two successive solutions coincide. If a unique solution exists, the iterations will always converge to that point.

This algebraic reconstruction algorithm generally called as algebraic reconstruction technique (ART), may further be classified into different categories depending upon the correction applied. Four classes of ART are mentioned below.

1. Mayinger ART
2. Gordon ART.
3. Gilbert ART
4. Anderson ART

In this problem, Mayinger ART has been used. In travelling from the source to the receiver, the ultrasonic ray can travel in a straight line or it can take a curved path depending on the difference in its velocities through the parent material and the insert material. If this difference exceeds 15%, taking recourse to ray bending gives better results than straight ray approach. In this problem ray-bending has been taken into consideration while tracing the path of the ultrasonic beam from the source to the receiver. Chapter 3 deals with that phenomenon.

MART

There are various variants of the ART algorithms depending on the way the corrections are applied. One such modified version is the MART, which is also known as the multiplicative ART. In MART, after every iteration, a new estimate of the field value is calculated by multiplying the previous value with a correction term, i.e.

$$S_j^{(k+1)} = CS_j^{(k)} \quad j = 1, 2, 3, \dots, N \quad (2.7)$$

where "C" is the correction term, and $S_j^{(k)}$ is the slowness value of the j^{th} pixel at the end of the k^{th} iteration. Again depending on the correction term, MART may be further classified into four classes. The underlying algorithm remains the same but the only difference lies in the correction term. The four algorithms along with the associated correction terms are provided below.

1. GBH MART

Gordon, Bender and Herman proposed this algorithm for tomographic applications. In this algorithm, the correction term is given by

$$C = 1 - \frac{\lambda}{(W_{ij})_{\max}} \left(1 - \frac{(\tau_i)_m}{(\tau_i)_c} \right) \text{if } (\tau_i)_c \neq 0, \text{and } W_{ij} \neq 0 \quad (2.8)$$

else

$$C=1$$

where,

λ is the relaxation parameter,

W_{ij} is the intercept made by the i^{th} ray in the j^{th} pixel.

$(W_{ij})_{\max}$ is the maximum of all intercepts made by the i^{th} ray.

$(\tau_i)_m$ and $(\tau_i)_c$ are the measured and calculated time of flight data respectively.

2. GH MART

This algorithm was proposed by Gordon and Herman. The correction term is given by,

$$C = 1 - \frac{\lambda W_{ij}}{(W_{ij})_{\max}} \left(1 - \frac{(\tau_i)_m}{(\tau_i)_c} \right) \text{if } (\tau_i)_c \neq 0, \text{and } W_{ij} \neq 0 \quad (2.9)$$

else

$$C=1$$

3. LENT MART

Lent has proposed another multiplicative updating scheme, in which the correction term is computed as,

$$C = \left(\frac{(\tau_i)_m}{(\tau_i)_c} \right)^{\lambda W_{ij}} \text{if } (\tau_i)_c \neq 0 \quad (2.10)$$

else

$$C=1$$

4. LENT MART2

A slight modification of the above algorithm leads to Lent MART2. Here the correction term is given as,

$$C = \left(\frac{(\tau_i)_m}{(\tau_i)_c} \right) \lambda W_y^* \text{ if } (\tau_i)_c \neq 0 \quad (2.11)$$

else

C=1

where

W_{ij}^* is given by W_{ij}/W_{max}

SIRT

The ART algorithms enjoy a rapid convergence in the root-mean-squared error criterion. However, the reconstructed images exhibit a very noisy salt-and-pepper characteristic. Smoother images are obtained by the simultaneous iterative reconstruction technique (SIRT) algorithm, in which the corrections in Eq.(2.16) are computed due to all the equations before altering any pixel values. Only then are the pixel values updated by their average corrections. This constitutes one iteration. In contrast with ART reconstructions, SIRT methods yield smoother images, although at the expense of slower convergence.

In ART algorithms, the salt-and-pepper noise is caused by the inconsistencies introduced in the set of equations by the approximations commonly used for W_{jk} . This results in computed ray sums in Eq.(2.14) being a poor approximation to the corresponding line integrals. The effect caused by such inconsistencies is exacerbated by the fact that as each equation corresponding to a ray in a projection is taken up, it changes some of the pixels just altered by the preceding equation in the same projection. The SIRT algorithm also suffers from these inconsistencies in the forward process (appearing in the computation of q_i in Eq.(2.14); but by the elimination of the continual pixel update as each new equation is taken up, smoother reconstructions can be obtained.

2.3 Computer Implementation of the procedure

Step1

An initial guess to the solution of the discussed system of equations is assumed. This guess, denoted by $x_1^{(0)}, x_2^{(0)}, \dots, x_N^{(0)}$, is represented vectorially by $\mathbf{x}^{(0)}$ in the N-dimensional space. This initial guess is projected on the hyperplane represented by the

first of the equations i.e. Eq (2.2) thus yielding $\mathbf{x}^{(1)}$. Then $\mathbf{x}^{(1)}$ is projected on the hyperplane represented by the second equation to yield $\mathbf{x}^{(2)}$, and this process is repeated till the entire set of equations is exhausted. When $\mathbf{x}^{(j-1)}$ is projected on the hyperplane represented by the j^{th} equation to yield $\mathbf{x}^{(j)}$, the process can be mathematically described by

$$\mathbf{x}^{(j)} = \mathbf{x}^{(j-1)} - \frac{(\mathbf{x}^{(j-1)} \cdot \mathbf{W}_j - p_j)}{\mathbf{W}_j \cdot \mathbf{W}_j} \mathbf{W}_j \quad (2.12)$$

where $\mathbf{W}_j = (w_{j1}, w_{j2}, \dots, w_{jN})$.

However, this equation cannot be used in its present form. The difficulty with using the above equation lies with the problem it poses in the calculation, storage and fast retrieval of the weight coefficients w_{ij} . For reconstructing an image on a 128x128 grid from 150 projections with 150 rays in each projection, the number of elements in the weight matrix becomes enormously large which can pose major problems in fast storage and retrieval in applications in which reconstruction speed is important.

To circumvent the implementation difficulties caused by the weight coefficients, recourse can be taken of different algebraic approaches. Many of these are approximations of Eq.(2.12).For a discussion of these approaches, Eq.(2.12) is first recast into the following equation.

$$\mathbf{x}_m^{(j)} = \mathbf{x}_m^{(j-1)} + \left[(p_j - q_j) / \sum_{k=1}^N W_{jk}^2 \right] W_{jm} \quad (2.13)$$

where ,

$$q_j = \mathbf{x}^{(j-1)} \cdot \mathbf{W}_j = \sum_{k=1}^N x_k^{(j-1)} W_{jk} \quad (2.14)$$

The underlying logic behind these equations is that, on projecting the $(j-1)^{\text{th}}$ solution onto the j^{th} hyperplane, the pixel value of the m^{th} element in the grid, whose current value is $x_m^{(j-1)}$, is obtained by correcting this current value by $\Delta x_m^{(j)}$, where

$$\Delta x_m^{(j)} = x_m^j - x_m^{(j-1)} = \frac{p_j - q_j}{\sum_{k=1}^N W_{jk}^2} W_{jm} \quad (2.15)$$

Here, as defined earlier, p_j is the measured ray-sum along the j^{th} ray. Similarly, q_j can be considered to be the computed ray-sum for the same ray based on the $(j-1)^{\text{th}}$ solution for the image pixel values. The correction Δx_m to the m^{th} cell is obtained by first calculating the difference between the measured ray-sum and the computed ray-sum, normalizing this difference by $\sum w_{jk}^2$, and then assigning this value to all the image cells in the j^{th} ray, each assignment being weighted by the corresponding w_{jm} .

In one approximation to Eq.(2.15), the w_{jk} are simply replaced by 1's and 0's, depending on whether the center of the k^{th} image cell is within the j^{th} ray. This makes the implementation easier, because such a decision can easily be made at computer run-time. Clearly in this case, the denominator in Eq.(2.15) can be replaced by N_j , which is the number of image cells whose centers are within the j^{th} ray. The correction to the m^{th} image cell from the j^{th} equation in Eq.(2.15) can now be written as

$$\Delta x_m^j = \frac{(p_j - q_j)}{N_j} \quad (2.16)$$

for all the cells whose centers are within the j^{th} ray. The approximation in Eq.(2.16), although easy to implement, may lead to artifacts in the reconstructed images if N_j is not a good approximation to the denominator of Eq.(2.15).

Step 2

The process of taking projections on different hyperplanes is continued until $x^{(M)}$ is obtained, which in turn is obtained by taking the projection on the last of the system of equations i.e. Eq.(2.4). This completes one cycle of this iterative procedure.

In steps 1 and 2, as each new equation starting from Eq.(2.2) and ending at Eq.(2.4) is taken up, the values of all the affected pixels are updated. In a related approach, which may lead to fewer artifacts, the changes in $\Delta x_m^{(j)}$ caused by the j^{th} equation in the system of equations, can again be computed. However, now the value of the m^{th} cell is not changed at this time. The cell values remain intact until all the equations are finished and then only at the end of each iteration the cell values are

changed, the change for each cell being the average value of all the computed changes for that cell.

Step 3

Iterations are continued by projecting $\mathbf{x}^{(M)}$ on the first hyperplane again. This process continues till all the hyperplanes have again been cycled through, resulting in $\mathbf{x}^{(2M)}$. The second iteration is started by projecting $\mathbf{x}^{(2M)}$ on to the first hyperplane, and so on. Iterations are stopped when the computed changes of the image cell values are negligible fractions of their current values.

2.4 Formulation of the present problem in the light of the algebraic reconstruction algorithm

The experiment consists of generating ultrasound and thereby sending the same through an isotropic material. The positions of the source and receiver are first fixed up according to the angle, which the ultrasonic ray takes in travelling through the medium. As already mentioned earlier in this chapter, a fan-beam configuration has been taken with five rays emanating from each point-source. Finally among these five rays, only one ray, which reaches nearest to the corresponding receiver position, is considered and the other four rays are discarded. Thus in the final analysis, one ray has been considered for a source-receiver pair. The algebraic reconstruction algorithm, which has been discussed in the previous sections of this chapter, is applied to reconstruct the slowness field in a slice-plane of the isotropic material. For isotropic materials, slowness is simply the inverse of the longitudinal sonic velocity through the medium. The projection data for this problem is the time of flight, i.e. the transit time between the source and the receiver. The iterative process starts from an initial approximation of slowness, S^0 , and the current iterate S^k is corrected to a new iterate S^{k+1} by taking into account only a single ray and changing the image values of the pixels through which the ray passes. The disparity between the measured time of flight, and the pseudo-projection data, also called the numerical time of flight, obtained from the current image S^k , is redistributed among the pixels falling in the path of the ray, proportionally to their weights, which are the intercepts that the ray makes with the pixels through which it passes. In this way, the pixel values along a

particular ray are corrected to conform to that measurement of the projection data without changing the rest of the image. The whole process is described mathematically as:

$$S_j^{(k+1)} = S_j^{(k)} + \frac{\tau_i - \langle w^i, S^k \rangle}{\| w^i \|^2} w^i \quad (2.17)$$

where,

$$\langle w^i, S^k \rangle = \sum_{j=1}^N W_j S_j^{(k)} \quad (2.18)$$

$$w^i = \sum_{j=1}^N W_j \quad (2.19)$$

and

$$\| w^i \|^2 = \langle w^i, w^i \rangle \quad (2.20)$$

Introducing the relaxation parameter, the modified step for updating the iterate can be expressed as

$$S_j^{(k+1)} = S_j^{(k)} + \lambda \frac{\tau_i - \langle w^i, S^k \rangle}{\| w^i \|^2} w^i \quad (2.21)$$

where, λ is the relaxation parameter, which is a real number, usually lying between 0 and 2.

If the correction is negative, it may happen that the calculated field of a reconstructed image is negative, in which case it is set to zero, as discussed by *Gordon*.

2.5 Closure

A description of the commonly applied tomographic algorithms has been presented in this chapter. The problem at hand has also been formulated in the light of these algorithms. The various steps involved in the computer implementation of these algorithms are also provided in this chapter.

Chapter 3

Ray-Bending and Edge-Detection

3.1 Introduction

The ultrasonic wave undergoes refraction when it encounters an inhomogeneity in its path of propagation. This phenomenon becomes more complex if there are more than one inhomogeneity present in a solid object. The use of digital ray tracing method has paved the way for the determination of the actual path of wave propagation between the source and the receiver under such condition. Using digital ray tracing method in conjunction with the algebraic reconstruction algorithms, it is possible to reconstruct either the slowness or the velocity field in a material with refraction artifacts.

3.2 Ultrasonic wave propagation

Ultrasonic waves of small amplitude propagate as linear elastic waves whose propagation through a medium results in particle oscillations about their equilibrium positions. In ideal liquids and gases only one mode of propagation exists. This longitudinal mode has particle displacements parallel to the direction of ultrasonic propagation. The ultrasonic velocity is governed by the compressibility of the materials and for these materials, is independent of propagation direction. Elastic solids can accommodate transverse waves (where the particle displacements are perpendicular to the direction of propagation), as well as longitudinal waves. The particle motions in elastic solids associated with these

bulk modes of propagation can be resolved into three perpendicular components, one longitudinal and two transverse to the direction of propagation.

Wave propagation in anisotropic solids

In anisotropic elastic solids, each of the three modes, one longitudinal and two transverse modes has its own characteristic velocity, although in isotropic solids the two transverse velocities degenerate into one. For anisotropic solids, the phase velocity (v) of the three possible bulk modes (quasi-longitudinal, fast and slow quasi-shear) in a direction defined by the unit propagation vector, \mathbf{n} , with components n_j , $j = 1,2,3$ can be found from the eigenvalues of the Christoffel equation given as follows:

$$(k^2 C_{ijkl} n_k n_l - \rho w^2 \delta_{ij}) d_j = 0 \quad i = 1,2,3. \quad (3.1)$$

where ρ is the density of the material, $k = w/v$, is the wave-number, w is the angular frequency, C_{ijkl} are the components of the elastic stiffness tensor, d_j , $j = 1,2,3$ are the components of the unit particle displacement vector, d , and δ_{ij} is the Kronecker delta. For a given propagation direction vector \mathbf{n} , the squares of the phase velocities of the bulk modes are obtained as the eigenvalues of Eq.(3.1). The particle displacement vector, d , of a bulk mode is obtained as a unit eigenvector for the phase velocity (eigenvalue) of the bulk mode. The slowness (or inverse velocity) surface gives the inverse phase velocity as a function of propagation direction and is independent of the angular frequency.

An important consequence of anisotropic wave propagation is that the energy of a wave packet does not necessarily propagate parallel to the direction of wave propagation, unlike in an isotropic media, where both directions are coincident. In a lossless medium, the energy or group velocity is perpendicular to the slowness surface. The powerflow angle defined as the angle between the energy velocity and the propagation direction depends on the shape of the slowness surface. The group velocity, which governs the speed of a modulated disturbance (i.e. a pulse), can be determined once the phase velocity and the displacement vector for a specific mode are known.

3.3 Reflection and transmission at an interface

When an ultrasonic wave propagating in a homogeneous medium passes through an interface at a normal incident angle where the velocity (i.e. the elastic constant and density) of the second medium is different (i.e. solid-solid or solid-liquid interface), the incident wave is reflected and transmitted without any change in the propagation direction. However, when the ultrasonic wave, propagating in a homogeneous medium passes through an interface at a non-normal incident angle, the incident wave is mode converted (a change in the nature of the wave motion) and refracted (a change in the direction of wave propagation). These phenomena may affect the entire beam or only a small portion of the beam and the sum total of the changes that occur at the interface depends on the angle of incidence and the velocity of the ultrasonic waves leaving the point of impingement on the interface. The reflection and refraction of these ultrasonic waves is governed by the acoustic analog of Snell's law (the ratio of the sine of the angle of incidence to the sine of the angle of reflection or refraction equals the ratio of the corresponding wave velocities). If two media are represented by 1 and 2, then Snell's law can be put in mathematical form as follows:

$$\frac{\sin \theta_1}{v_1} = \frac{(\sin \theta_2)_l}{(v_2)_l} = \frac{(\sin \theta_2)_s}{(v_2)_s} \quad (3.2)$$

where θ_1 , $(\theta_2)_l$ and $(\theta_2)_s$ are the ray angles with respect to the surface normal and v_1 , $(v_2)_l$ and $(v_2)_s$ are the velocities of the longitudinal wave in the first medium, the longitudinal and shear wave velocities in the second medium. The phenomenon has been pictorially depicted in Fig.(3.1). However, Snell's law is equally valid for a solid-solid interface. For the problem at hand, a solid-solid interface is present. If the angle of incidence is small, the incident wave undergoes a mode conversion at the interface, resulting in the simultaneous propagation of longitudinal and shear waves in the second medium. If the angle of incidence is increased, the direction of the refracted longitudinal wave will approach the plane of the interface. At the first critical incidence angle, the refracted longitudinal wave will disappear leaving only a refracted (mode converted) shear wave to propagate in the second medium. Now if the incidence angle is increased beyond this critical value, the direction of this refracted shear wave will approach the plane of the interface. At this second critical incidence angle, the refracted shear wave will disappear.

and the incident wave is only reflected at an angle equal to the incident angle. This methodology applies to any interface, i.e. liquid-solid, solid-solid and solid-liquid.

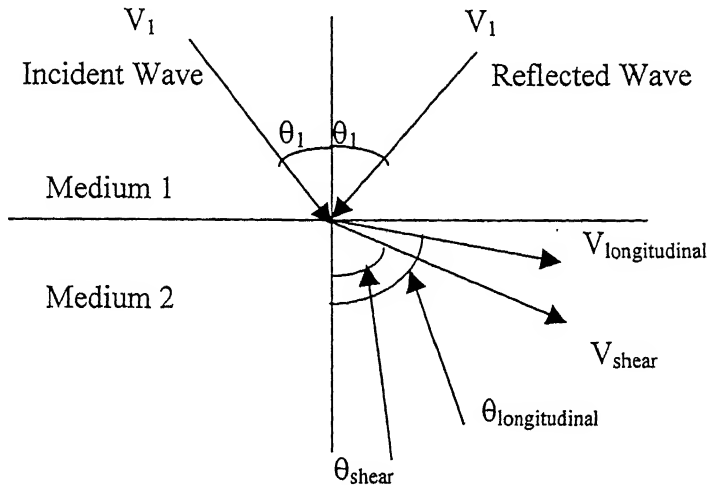


Figure (3.1) Reflected and refracted rays at a solid-solid interface

3.4 Ultrasonic ray theory

Geometrical acoustics describe the propagation behaviour of acoustic rays in liquid and solid bodies. In the development of ultrasonic sensor methodology for reliable image reconstruction using refracted ray paths, the sometimes severe nature of ray bending implies a need for precise knowledge of ray paths, particularly when time of flight data is needed.

In general, there are two methods to determine the ray paths between two points; shooting and bending. The shooting method uses an iterative procedure to determine the ray path from a source point by solving the differential equations that follow from ray theory for different initial conditions until the ray arrives at the receiver point. Ray bending uses Fermat's principle as a starting point. Ray bending is assumed to occur at a refraction artifact. The effect of ray bending cannot be ignored when the sonic velocity difference between the base and the insert material is over 15%.

Both methods have certain limitations. By shooting a fan of rays from the source, an impression of the wave field can be obtained. However, convergence problems are known to occur, frequently in three dimensions. Also shooting will not find diffracted ray paths or ray paths in shadow zones, where ray theory breaks down. With bending, every ray path satisfying Snell's law and Fermat's principle can be found, even a

diffracted one, but only for one source-receiver pair at a time. In the present work the refracted ray paths have been determined using Snell's law.

3.5 Image Analysis and Edge Detection

The reconstructed image obtained is refined using various edge detection techniques. Changes or discontinuities in an image amplitude attribute such as luminance or tristimulus value are fundamentally important primitive characteristics of an image because they often provide an indication of the physical extent of objects within the image. Local discontinuities in image luminance from one level to another are called luminance edges. In this section, several techniques for detecting the three basic types of discontinuities in a digital image: (1) points (2) lines and (3) edges will be discussed. The most common way to look for discontinuities is to run a mask through the image. This procedure involves computing the sum of products of the coefficients with the pixel values contained in the region encompassed by the mask. Thus, the response of the mask at any point in the image is given as follows:

$$R = w_1 z_1 + w_2 z_2 + \dots + w_9 z_9 \quad (3.3)$$

where z_i is the value of the pixel associated with the 3×3 mask coefficient w_i . The response of the mask is defined with respect to its center location. When the mask is centered on a boundary pixel, the response is computed by using the appropriate partial neighbourhood

3.5.1 Point detection

The detection of isolated points in an image is straightforward. A point is said to be detected at the location on which a mask is centered if $|R| > T$, where T is a nonnegative threshold, and R is given by Eq.(3.3). Thus the underlying idea here is to compute the weighted differences between the center point and its neighbours. The idea is that the pixel value of an isolated point will be quite different from the pixel value of its neighbours.

3.5.2 Line detection

The next level of complexity involves the detection of lines in an image. The phenomenon is best demonstrated by considering the four simple masks given below.

-1	-1	-1
2	2	2
-1	-1	-1

Horizontal

-1	-1	2
-1	2	-1
2	-1	-1

+45 degree

-1	2	-1
-1	2	-1
-1	2	-1

Vertical

2	-1	-1
-1	2	-1
-1	-1	2

-45 degree

If the first mask were moved around an image, it would respond more strongly to lines oriented horizontally. With constant background, the maximum response would result when the line passed through the middle row of the mask. A similar logic would reveal that the second of the masks shown above responds best to lines oriented at 45°; the third mask to vertical lines; and the fourth mask to lines in the -45° direction. These directions

3.5.2 Line detection

The next level of complexity involves the detection of lines in an image. The phenomenon is best demonstrated by considering the four simple masks given below.

-1	-1	-1
2	2	2
-1	-1	-1

Horizontal

-1	-1	2
-1	2	-1
2	-1	-1

+45 degree

-1	2	-1
-1	2	-1
-1	2	-1

Vertical

2	-1	-1
-1	2	-1
-1	-1	2

-45 degree

If the first mask were moved around an image, it would respond more strongly to lines oriented horizontally. With constant background, the maximum response would result when the line passed through the middle row of the mask. A similar logic would reveal that the second of the masks shown above responds best to lines oriented at 45°; the third mask to vertical lines; and the fourth mask to lines in the -45° direction. These directions

can be easily established by noting that the preferred direction of each mask is weighted with a larger coefficient (i.e. 2) than other possible directions.

Let R_1 , R_2 , R_3 and R_4 denote the responses of the masks shown above, where R has been defined in Eq.(3.3). For example, after running all the masks through an image if at a certain point in the image, $|R_1| > |R_j|$, for $j = 2,3,4$ that particular point is said to be more likely associated with a horizontal line.

3.5.3 Edge detection

Although point and line detection certainly are important elements of image segmentation, edge detection is by far the most common approach for detecting meaningful discontinuities in an image represented by pixel values (gray levels). The reason is that isolated points and thin lines are not frequent occurrences in most practical applications.

An edge is the boundary between two regions with relatively distinct gray-level properties. The commonly applied segmentation techniques are valid on the assumption that the regions in question are sufficiently homogeneous so that the transition between two regions can be determined on the basis of gray-level discontinuities alone.

Basically, the idea underlying most edge-detection techniques is the computation of a local derivative operator. Actually, the magnitude of the first derivative can be used to detect the presence of an edge in the image and the sign of the second derivative can be used to determine whether an edge pixel lies on the dark or light side of an edge. The second derivative has always a zero crossing at the midpoint of a transition in gray level. The zero crossings provide a powerful approach for locating edges in an image. This is in context to a one-dimensional horizontal profile. However, a similar argument applies to an edge of any orientation in an image. A profile perpendicular to the edge direction at any desired point can be defined always and the result can be interpreted in similar lines to the horizontal unidimensional profile. The first derivative at any point in an image is obtained by using the magnitude of the gradient at that point. The second derivative is similarly obtained by using the Laplacian.

First order derivative edge detection

There are two fundamental methods for generating first order derivative edge gradients. One method involves generation of gradients in two orthogonal directions in an image, while the other utilizes a set of directional derivatives.

Orthogonal gradient generation

An edge in a continuous domain edge segment $F(x,y)$, can be detected by forming the continuous one-dimensional gradient $G(x,y)$ along a line normal to the edge slope, which is at an angle θ with respect to the horizontal axis. If the gradient is sufficiently large, i.e. above some threshold value, an edge is deemed present. The gradient along the line normal to the edge slope can be computed in terms of the derivatives along orthogonal axes according to the following equation as follows:

$$G(x,y) = \frac{\Delta F(x,y)}{\Delta x} \cos \theta + \frac{\Delta F(x,y)}{\Delta y} \sin \theta \quad (3.4)$$

Thus an edge gradient $G(j,k)$ can be written in terms of a row edge gradient $G_R(j,k)$ and a column gradient $G_C(j,k)$. The spatial gradient amplitude is given by

$$G(j,k) = \left\{ [G_R(j,k)]^2 + [G_C(j,k)]^2 \right\}^{1/2} \quad (3.5)$$

For computational efficiency the gradient amplitude is sometimes approximated by the magnitude combination

$$G(j,k) = |G_R(j,k)| + |G_C(j,k)| \quad (3.6)$$

The orientation of the spatial gradient with respect to the row axis is

$$\theta(j,k) = \tan^{-1} \left\{ \frac{G_C(j,k)}{G_R(j,k)} \right\} \quad (3.7)$$

The remaining issue for discrete domain orthogonal gradient generation is to choose an accurate discrete approximation to the continuous differentials along the horizontal and vertical directions.

The simplest method of discrete gradient generation is to form the running difference of pixels along rows and columns of the image. The row gradient and column gradient are defined as

$$G_R(j, k) = F(j, k) - F(j, k-1) \quad (3.8)$$

$$G_C(j, k) = F(j, k) - F(j+1, k) \quad (3.9)$$

These definitions of row and column gradients, and subsequent extensions are so chosen such that G_R and G_C are positive for an edge that increases in amplitude from left-to-right and from bottom-to-top in an image.

Diagonal edge gradients can be obtained by forming running differences of diagonal pairs of pixels. This is the basis of the Roberts cross difference operator, which is defined in magnitude form as

$$G(j, k) = |G_1(j, k)| + |G_2(j, k)| \quad (3.10)$$

and in square root form as

$$G(j, k) = \left\{ [G_1(j, k)]^2 + [G_2(j, k)]^2 \right\}^{1/2} \quad (3.11)$$

where

$$G_1(j, k) = F(j, k) - F(j+1, k+1) \quad (3.12)$$

$$G_2(j, k) = F(j, k+1) - F(j+1, k) \quad (3.13)$$

The edge orientation with respect to the row axis is

$$\theta(j, k) = \frac{\pi}{4} + \tan^{-1} \left[\frac{G_2(j, k)}{G_1(j, k)} \right] \quad (3.14)$$

Visually, the objects in an image appear to be better distinguished with the Roberts square root gradient than with the magnitude gradient.

Prewitt has introduced a 3x3 pixel edge gradient operator. The Prewitt square root edge gradient is defined as

$$G(j, k) = \left\{ [G_R(j, k)]^2 + [G_C(j, k)]^2 \right\}^{1/2} \quad (3.15)$$

with

$$G_R(j, k) = \frac{1}{k+2} [(A_2 + kA_3 + A_4) - (A_0 + kA_1 + A_6)] \quad (3.16)$$

$$G_C(j, k) = \frac{1}{k+2} [(A_0 + kA_1 + A_2) - (A_6 + kA_5 + A_4)] \quad (3.17)$$

where $k = 1$ and A_i are given as follows.

A_0	A_1	A_2
A_7	$F(j, k)$	A_3
A_6	A_5	A_4

Numbering convention for 3x3 edge detection operators.

In this formulation the row and column gradients are normalized to provide unit gain positive weighted and unit gain negative weighted averages about a separated edge position.

The Sobel edge detector, which is used in the present problem, differs from the Prewitt edge detector in that the values of the north, south, east and west pixels are doubled, i.e. $k=2$. The motivation for this weighting is to give equal importance to each pixel in terms of its contribution to the spatial gradient. Another idea is to give north, south, east and west weightings a value of 1.414 so that the gradient is the same for horizontal, vertical and diagonal edges. The Prewitt operator is more sensitive to horizontal and vertical edges than diagonal edges; the reverse is true for the Sobel operator.

A limitation common to the edge detection operators is their inability to detect accurately edges in high-noise environments. This problem can be alleviated by properly extending the size of the neighbourhoods over which the differential gradients are computed.

3.5.4 Threshold selection

After the edge gradient is performed for the differential edge detection methods, the gradient is compared to a threshold to determine if an edge exists. The threshold value determines the sensitivity of the edge detector. For noise-free images the threshold can be chosen such that all amplitude discontinuities of a minimum contrast level are detected as edges and all others are called non-edges. With noisy images, threshold selection becomes a tradeoff between missing valid edges and designating noise-induced false edges.

3.5.5 Second order derivative edge detection

Second order derivative edge detection techniques employ some form of spatial second order differentiation to accentuate edges. An edge is marked if a significant spatial change occurs in the second derivative. Two types of second order derivative methods are generally used: (1) Laplacian and (2) Directed second derivative.

Laplacian generation

The edge Laplacian of an image function $F(x,y)$ in the continuous domain is defined as

$$\frac{-\delta^2 F(x,y)}{\delta x^2} + \frac{-\delta^2 F(x,y)}{\delta y^2} \quad (3.18)$$

The Laplacian $G(x,y)$ is zero if $F(x,y)$ is constant or changing linearly in amplitude. If the rate of change of $F(x,y)$ is greater than linear, $G(x,y)$ exhibits a sign change at the point of inflection of $F(x,y)$. The zero crossing of $G(x,y)$ indicates the presence of an edge.

In the discrete domain the simplest approximation to the continuous Laplacian is to compute the difference of slopes along each axis.

$$G(j,k) = [F(j,k) - F(j,k-1)] - [F(j,k+1) - F(j,k)] + [F(j,k) - F(j+1,k)] - [F(j-1,k) - F(j,k)] \quad (3.19)$$

In the present problem, the above approximation has been taken for the continuous Laplacian.

Directed second order derivative generation

Laplacian edge detection techniques employ rotationally invariant second order differentiation to determine the existence of an edge. The direction of the edge can be ascertained during the zero crossing detection process. An alternate approach is to first estimate the edge direction, and then compute the one-dimensional second order derivative along the edge direction. A zero crossing of the second order derivative specifies an edge.

The directed second order derivative of a continuous domain image $F(x,y)$ along a line at an angle α with respect to the horizontal axis is given by

$$F''(x, y) = \frac{\partial^2 F(x, y)}{\partial x^2} \cos^2 \theta + \frac{\partial^2 F(x, y)}{\partial x \partial y} \sin \theta \cos \theta + \frac{\partial^2 F(x, y)}{\partial y^2} \sin^2 \theta \quad (3.20)$$

Unlike the Laplacian, the directed second order derivative is a nonlinear operator. A key factor in the utilization of the directed second order derivative edge detection method is the ability to accurately determine its suspected edge direction.

3.6 Closure

In this chapter ray bending has been discussed. Snell's law, which dictates the direction taken up by the ray when it encounters an inhomogeneity in its path of propagation, has also been taken up. Finally various image segmentation techniques, namely, point detection, line detection and most importantly edge detection has been discussed at length. The edge detection techniques, which have been used in this present work, have also been mentioned.

Chapter 4

Results and discussion

4.1 Introduction

In the present work, Mayinger ART algorithm has been used for the reconstruction of the tomographic images. Here essentially the slowness (inverse of ultrasonic velocity) distribution in the domain from numerous projection data are computed. The projection data basically consists of measuring the time of flight from the source to the receiver. Curved ray approach has been used to compute the ray paths. The acoustic analogue of Snell's law has been used to ascertain the path taken by the ray after it encounters a refraction artifact.

The present study has been conducted for three different combinations of parent material and insert materials. They are (1) Steel with Aluminium insert (2) Steel with Nickel insert and (3) Steel with brass insert. Three different types of defect geometries have been considered, namely, square, circular and elliptical. The quality of reconstruction has been studied with respect to the contrast of the base and insert materials, i.e. the relative difference in wave velocities between the defect and the base material. The quality of reconstruction has also been found for values of relaxation parameters lying within the range 0.1 to 0.4. All the reconstructed images have been shown for these values of the relaxation parameter only. The following table lists the properties of the materials, which have been used in this work.

Serial Number	Base material	Insert material	Velocity of sound in base material	Velocity of sound in insert material	Projection data type
1	Steel	Aluminium	5160 m/sec	5050 m/sec	4-view
2	Steel	Nickel	5160 m/sec	4820 m/sec	4-view
3	Steel	Brass	5160 m/sec	3700 m/sec	4-view

Table 4.1 Properties of the base material and the insert materials.

4.2 Details of Test cases

In the present work, the tomographic reconstruction of square, circular and elliptical defects have been carried out for three different combinations of parent material and the insert material. All the reconstructions have been carried out taking a 4-view projection.

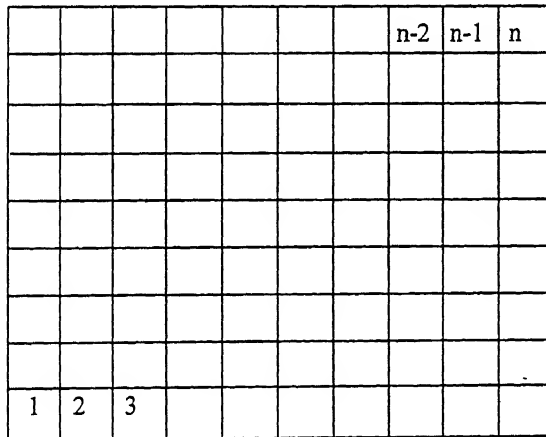


Figure 4.1 Grid for discretizing the domain

The iterative reconstruction methods require the discretization of the domain to be represented by a square or rectangular grid. For the problem at hand, a 20×20 square grid has been taken. However, for clarity, a 10×10 grid has been shown in Figure 4.1. The individual elements in the grid are referred to as pixels. The pixels were numbered from 1 to 400. Here the analysis is carried out by taking a four-view projection. The rays of

sound energy were sent through the sample at four different angles, namely, 0° , 45° , 90° and 135° with respect to the positive X-axis. While ultrasound traverses through the material, the rays pass through the various pixels. When the i^{th} ray passes through the j^{th} pixel, the length of the intercept made by the i^{th} ray in the j^{th} pixel is denoted by w_{ij} , which is popularly called the weight. This has been depicted in Figure 4.2. In the present work, 20 rays each inclined at 0° and 90° have been taken along with 40 rays each inclined at 45° and 135° respectively. Thus in all, 120 rays have been considered for the image reconstruction. However, while collecting simulated time of flight data for four transmitter-receiver locations at 45° and 135° , the rays starting from those particular transmitter locations have not reached the corresponding receiver locations due to large refraction at the intervening defects. Thus, 112 rays have been considered finally.

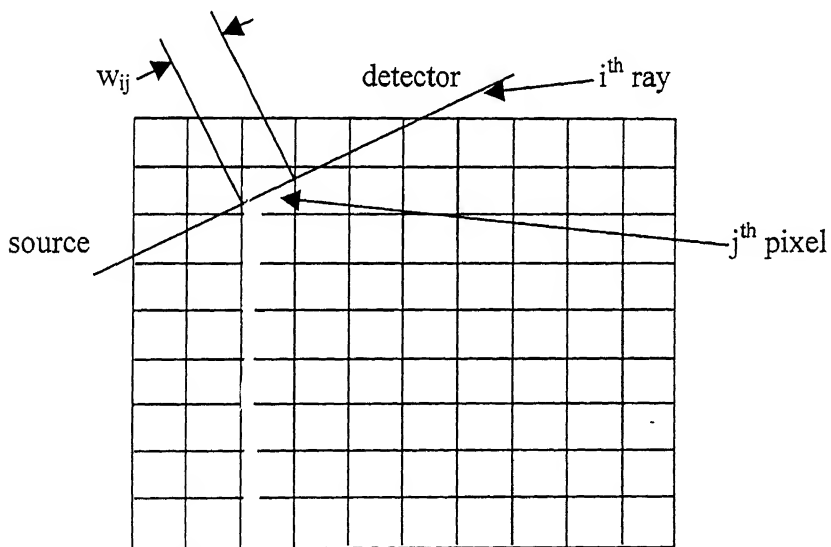


Figure 4.2. Intercept made by the i^{th} ray in the j^{th} pixel

In this problem, to trace the correct ray, a set of five rays emanating from each point source, with an angular spacing of 1.25° between two consecutive rays has been taken. Here are the details of the rays along each view.

1. Ray-Paths along 0° direction (x-axis)

In this view, in all 20 data have been collected from 20 ray-paths, each source being located inside a pixel situated in the first column of the grid. The spacing between the rays of two consecutive sources has been taken as unity. The source points act as the transmitter points, while the corresponding receiver points are situated exactly opposite to the transmitter points. A set of five individual rays are sent out from a source at a spatial separation of 1.25° . Typical ray-paths for three 0° fan-beams, one passing through the Nickel insert, the other two just lying on either side of the insert are shown in Figure 4.4. The insert is circular in shape and the plot of rays after 5 iterations is shown in the figure. From the plot it can be observed that the central fan-beam passes through the insert where there is a marked deviation of the rays. Inside the insert, the rays are more closely spaced than in the region outside.

2. Ray-Paths along 90° direction (y-axis)

In this view also, in all 20 data have been collected from 20 ray-paths, each source being located inside a pixel situated in the first row of the grid. Here also the spacing between the rays of two consecutive sources has been taken to be unity. The source points act as the transmitter points, while the corresponding receiver points are situated exactly opposite to the transmitter points. A set of five individual rays are sent out from a source at a spatial separation of 1.25° . Typical ray-paths for three 90° fan-beams, one passing through the Aluminium insert, the other two just lying on either side of the insert are shown in Figure 4.3. The insert is circular in shape and the plot of rays after 5 iterations is shown in the figure. Here inside the insert, the rays are not so closely spaced as in the previous case.

3. Ray-Paths along 45° direction

For this configuration 40 source points have been considered. Here the transmitter points or the source points as they are referred to here, are located both on the left vertical and bottom horizontal edges of the scanned specimen. The corresponding receiver locations are on the top horizontal and right vertical edges of the sample. The spacing between the

rays of two consecutive sources is now 0.7071 units. A set of five individual rays are sent out from a source at a spatial separation of 1.25° . Out of these five rays, the ray which reaches closest to the corresponding receiver position is taken and the rest are discarded. However, while collecting simulated time of flight data for four transmitter-receiver locations, the rays starting from those particular transmitter locations have not reached the corresponding receiver locations due to large refraction at the intervening defects. Thus, 36 rays have been considered finally. Typical ray-paths for three 45° fan-beams, one passing through the Brass insert, the other two just lying on either side of the insert are shown in Figure 4.5. From the figure, it can be clearly observed that the central fan-beam passes through the insert for which there is marked deviation for all the rays. The insert is circular in shape and the plot of rays after 5 iterations is shown in the figure.

4. Ray-paths along 135° direction

For this configuration also, 40 source points have been considered. Here the transmitter points or the source points as they are referred to here, are located both on the right vertical and bottom horizontal edges of the scanned specimen. The corresponding receiver locations are on the top horizontal and left vertical edges of the sample. Here also, the spacing between the rays of two consecutive sources is 0.7071 units. A set of five individual rays are sent out from a source at a spatial separation of 1.25° . Out of these five rays, the one which reaches closest to the corresponding receiver position is taken and the rest are discarded. Here also, due to the absence of time-of-flight data for four positions of the source point, in the final analysis only 36 data have been taken into consideration.

4.3 Image Reconstruction

In Figures 4.3-4.5, typical ray-paths for three sets of rays, one at 0° , the other at 90° and the third one at 45° are shown. One set is so chosen that it passes through the insert and the other two lie just on either side of the insert. The insert is circular in shape. There is a clear deviation of the rays when they pass through the insert indicating its presence in the

base material. The deviations are marked for the fan-beam inclined at 45° . All the plots have been taken after 5 iterations. Besides that, in Figures 4.6 and 4.7, the entire ray-paths are plotted, one for circular Aluminium insert and the other for circular Nickel insert. The plots are taken after 10 iterations. From Figures 4.3-4.5, it can be clearly observed that the central set of rays is so chosen that it entirely passes through the circular insert. Also in all the three cases, the deviation suffered by all the rays constituting the central set is the maximum, thus clearly indicating the presence of the insert in that region. Some of the typical slowness values obtained after a few iterations are shown in section 4.4. Though the order of the slowness matrix is 20×20 , only a 10×10 submatrix has been shown here.

4.3.1 Images obtained without ray bending consideration

Several images obtained without using curved ray approach have been shown in Figures 4.10-4.12 for the purpose of comparison with images obtained using ray bending. The images have been shown for all the three defect geometries taken. The difference in the quality of reconstruction is about 3% in terms of the normalized RMS errors for the Aluminium and Nickel inserts. In other words, this difference is quite acceptable because of the small difference in longitudinal sonic velocities between them and the base material i.e. Steel. However, the difference is much higher, about 5% for the case of Brass insert because there is more than 20% velocity difference of sound through Steel and Brass. Thus for Brass, the reconstructed images are of inferior quality for all the types of defect geometries.

4.3.2 Images obtained with ray bending consideration

The images obtained using ray bending are much superior than the same obtained without using ray bending. This is proved by the quality of reconstructed images. Also the normalized RMS errors are consistently lower by about 3% for all the defect geometries considered. However, the errors are about 5% lower for the case of Brass insert. For Brass insert though, ray bending consideration fails to produce superior images because of the high difference in longitudinal sonic velocity (20%) between Steel and Brass. But the quality of reconstruction is definitely better with ray bending consideration for all the

insert geometries. All the reconstructed images have been shown for four values of the relaxation parameter, namely, 0.1, 0.2, 0.3 and 0.4. The reconstruction is found to be best for values of relaxation parameter lying within this range. The reconstructed images obtained are also compared with the contour plots obtained for all the three defect geometries. The contour plots agree quite satisfactorily with the reconstructed images. Figures 4.13-4.24 show the images obtained using Aluminium insert, the first four showing the images for the square insert for four values of the relaxation parameter, the next four showing the same for the circular insert and the last four for the elliptical insert. The contour plots have been immediately provided after that in Figures 4.25-4.27 for the purpose of comparison with the actual images. Figures 4.28-4.39 show the images for the Nickel insert, the first four for the square insert, the next four for the circular insert and ending with the elliptical insert. Figures 4.40-4.51 show the same for the Brass insert in the same order.

4.4 Slowness values

Some representative values of slowness are shown for the case of circular Aluminium insert in Steel. Though the order of the slowness matrix is 20x20, a 10x10 submatrix is shown here. These values are as follows:

220.0725	242.2074	171.4287	156.5328	226.5117	247.9110	191.4956	153.7925	238.3172	212.6100
231.8917	181.8477	217.9228	204.4597	222.1963	204.0383	204.4881	201.2777	188.7148	237.0013
215.2587	245.4265	248.1114	251.5816	177.6984	170.6863	212.2036	234.5763	240.6320	228.3982
225.0943	258.0464	275.3279	231.8135	193.9398	177.7762	194.0678	237.1187	207.2527	185.5086
314.3125	275.8070	200.1192	165.4211	170.3677	178.5341	150.6968	134.6873	260.5496	233.4836
301.7101	281.7370	212.8128	161.6447	176.8761	171.0957	140.3271	126.5760	151.0003	240.6375
257.1631	319.7945	234.7083	185.6201	174.7852	167.1565	147.0800	134.9354	144.4117	184.5325
203.7310	307.8354	264.7107	310.0605	193.8991	203.8077	238.4700	234.6395	164.0039	162.8761
308.3214	245.9457	236.8223	274.0878	254.9149	244.1753	235.1453	238.4317	237.9478	231.5922
282.0224	234.3150	199.1402	222.6359	283.1949	243.8067	160.8466	148.9963	232.9315	256.5932

The values shown are obtained after 10 iterations.

4.5 RMS error

The following tables give the values of the normalized RMS errors for different values of the relaxation parameter and for different combinations of the insert and the base material. The RMS error measures the deviation of the reconstructed field from the exact field. It is defined as:

$$E_{RMS} = \sqrt{\frac{\sum_{i=1}^N (s_{ia} - s_{ir})^2}{N}} \times 100$$

where, s_{ia} and s_{ir} are the actual and reconstructed slowness values of the i^{th} pixel respectively. N is the total number of pixels. $(s_{\max})_a$ and $(s_{\min})_a$ are the actual maximum and minimum of all pixel values and E_{RMS} is the RMS error.

Serial Number	Relaxation Parameter (λ)	Number of iterations	Normalized RMS error
1	0.100	450	18.136
2	0.150	425	18.812
3	0.190	403	18.818
4	0.200	400	18.761
5	0.250	363	18.323
6	0.280	341	18.519
7	0.300	323	18.131
8	0.345	301	18.751
9	0.348	283	18.121
10	0.350	250	18.032
11	0.371	210	18.161
12	0.380	203	18.321
13	0.400	178	18.112
14	0.500	253	18.891
15	1.000	358	19.121
16	1.500	316	19.361
17	1.800	173	19.034

Table 4.2 showing normalized RMS errors of the reconstructed images for square Aluminium insert implanted in steel from 4-view projection data with different relaxation parameters.

Serial Number	Relaxation Parameter (λ)	Number of iterations	Normalized RMS error
1	0.100	437	17.675
2	0.150	417	17.234
3	0.200	356	17.060
4	0.250	323	16.580
5	0.300	265	18.123
6	0.350	234	17.451
7	0.400	179	17.231
8	0.450	145	16.890
9	0.500	132	18.012
10	0.550	118	17.941
11	0.600	102	17.894
12	0.650	96	18.034
13	0.700	89	18.145

Table 4.3 showing normalized RMS errors of the reconstructed images for circular Aluminium insert implanted in steel from 4-view projection data with different relaxation parameters.

Serial Number	Relaxation Parameter (λ)	Number of iterations	Normalized RMS error
1	0.100	421	17.565
2	0.150	411	17.452
3	0.200	373	17.160
4	0.250	306	16.280
5	0.300	279	18.156
6	0.350	251	16.347
7	0.400	192	16.938
8	0.450	163	17.003
9	0.500	146	17.812
10	0.550	131	17.976
11	0.600	112	17.954
12	0.650	104	17.937
13	0.700	98	18.578

Table 4.4 showing normalized RMS errors of the reconstructed images for elliptical Aluminium insert implanted in steel from 4-view projection data with different relaxation parameters.

Serial Number	Relaxation Parameter (λ)	Number of iterations	Normalized RMS error
1	0.100	439	18.178
2	0.150	427	18.341
3	0.190	413	18.564
4	0.200	395	18.265
5	0.250	378	18.127
6	0.280	356	18.783
7	0.300	334	18.451
8	0.345	313	18.129
9	0.348	292	17.621
10	0.350	261	17.932
11	0.371	223	17.947
12	0.380	212	18.674
13	0.400	194	18.546
14	0.500	245	18.451
15	1.000	349	18.821
16	1.500	312	19.869
17	1.800	181	18.960

Table 4.5 showing normalized RMS errors of the reconstructed images for square Nickel insert implanted in steel from 4-view projection data with different relaxation parameters.

Serial Number	Relaxation Parameter (λ)	Number of iterations	Normalized RMS error
1	0.100	415	17.673
2	0.150	400	17.341
3	0.200	385	17.762
4	0.250	331	16.897
5	0.300	290	17.756
6	0.350	267	16.367
7	0.400	224	17.031
8	0.450	178	16.987
9	0.500	161	17.413
10	0.550	149	18.098
11	0.600	124	17.786
12	0.650	112	18.005
13	0.700	107	18.737

Table 4.6 showing normalized RMS errors of the reconstructed images for circular Nickel insert implanted in steel from 4-view projection data with different relaxation parameters.

Serial Number	Relaxation Parameter (λ)	Number of iterations	Normalized RMS error
1	0.100	421	17.112
2	0.150	411	17.542
3	0.200	389	17.983
4	0.250	356	17.009
5	0.300	311	17.341
6	0.350	278	16.876
7	0.400	233	16.945
8	0.450	209	17.114
9	0.500	187	17.453
10	0.550	168	18.213
11	0.600	145	17.981
12	0.650	123	17.969
13	0.700	119	18.236

Table 4.7 showing normalized RMS errors of the reconstructed images for elliptical Nickel insert implanted in steel from 4-view projection data with different relaxation parameters.

Serial Number	Relaxation Parameter (λ)	Number of iterations	Normalized RMS error
1	0.100	476	18.213
2	0.150	453	18.986
3	0.190	411	18.453
4	0.200	397	18.342
5	0.250	376	19.112
6	0.280	361	18.897
7	0.300	316	17.985
8	0.345	297	18.156
9	0.348	286	18.211
10	0.350	265	17.967
11	0.371	243	18.673
12	0.380	221	19.096
13	0.400	197	18.543
14	0.500	231	19.003
15	1.000	344	19.311
16	1.500	326	19.278
17	1.800	201	18.891

Table 4.8 showing normalized RMS errors of the reconstructed images for square Brass insert implanted in steel from 4-view projection data with different relaxation parameters.

Serial Number	Relaxation Parameter (λ)	Number of iterations	Normalized RMS error
1	0.100	432	17.245
2	0.150	419	17.678
3	0.200	396	18.007
4	0.250	371	16.983
5	0.300	341	17.376
6	0.350	309	16.908
7	0.400	276	17.112
8	0.450	245	17.456
9	0.500	207	17.765
10	0.550	189	18.115
11	0.600	156	18.167
12	0.650	131	18.004
13	0.700	120	18.184

Table 4.9 showing normalized RMS errors of the reconstructed images for circular Brass insert implanted in steel from 4-view projection data with different relaxation parameters.

Serial Number	Relaxation Parameter (λ)	Number of iterations	Normalized RMS error
1	0.100	443	17.111
2	0.150	431	17.786
3	0.200	404	17.984
4	0.250	398	17.009
5	0.300	367	17.650
6	0.350	321	17.116
7	0.400	287	16.981
8	0.450	273	17.237
9	0.500	231	17.874
10	0.550	212	18.278
11	0.600	189	18.347
12	0.650	157	17.783
13	0.700	134	18.229

Table 4.10 showing normalized RMS errors of the reconstructed images for elliptical Brass insert implanted in steel from 4-view projection data with different relaxation parameters.

Serial Number	Relaxation Parameter (λ)	Number of iterations	Normalized RMS error
1	0.100	443	21.211
2	0.150	431	20.734
3	0.200	404	19.453
4	0.250	398	19.006
5	0.300	367	20.451
6	0.350	321	21.115
7	0.400	287	21.145
8	0.450	273	20.931
9	0.500	231	19.567
10	0.550	212	19.341
11	0.600	189	19.113
12	0.650	157	21.340
13	0.700	134	21.098

Table 4.11 showing normalized RMS errors of the reconstructed images for circular Brass insert implanted in steel from 4-view projection data with different relaxation parameters using straight ray assumption. The normalized errors are consistently higher in this case suggesting poorer reconstruction

Serial Number	Relaxation Parameter (λ)	Number of iterations	Normalized RMS error
1	0.100	411	20.156
2	0.150	402	19.113
3	0.200	389	21.453
4	0.250	378	21.005
5	0.300	361	20.568
6	0.350	343	19.456
7	0.400	292	21.317
8	0.450	265	20.561
9	0.500	223	19.908
10	0.550	207	20.231
11	0.600	191	21.341
12	0.650	151	20.567
13	0.700	137	20.213

Table 4.12 showing normalized RMS errors of the reconstructed images for elliptical Brass insert implanted in steel from 4-view projection data with different relaxation parameters using straight ray assumption. The normalized errors are consistently higher in this case suggesting poorer reconstruction

Number of iterations	Running time for the code (straight ray approach)	Running time for the code (curved ray approach)
50	20 minutes	2 hours
100	45 minutes	4 hours
150	60 minutes	5.5 hours
200	90 minutes	8 hours
250	120 minutes	10 hours

Table 4.13 showing a comparison of the times taken to execute the code with and without ray bending for various iterations

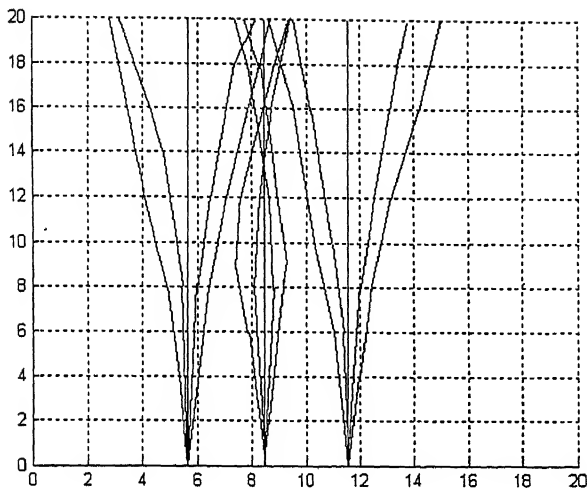


Figure 4.3 Ray-paths for three 90° fan-beams, one passing through the insert, the other two just lying on either side of the insert. The plot is for circular Aluminium insert

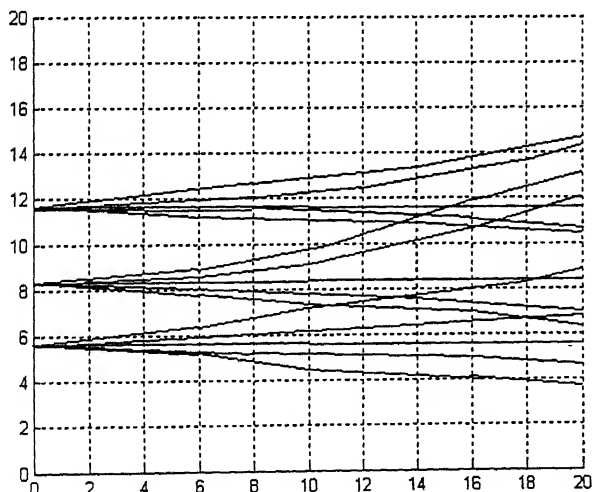


Figure 4.4 Ray-paths for three 0° fan-beams, one passing through the insert, the other two just lying on either side of the insert. The plot is for circular Nickel insert

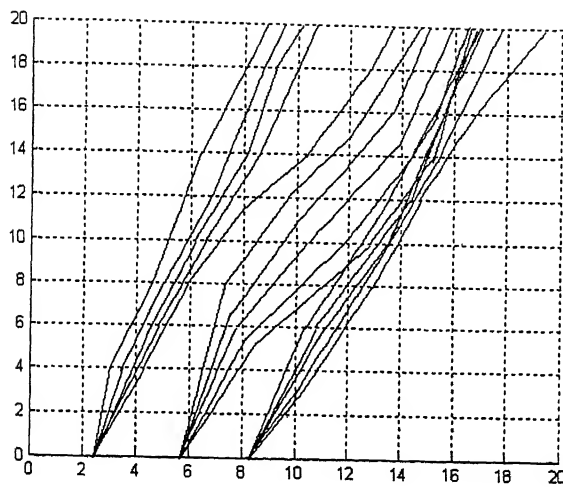


Figure 4.5 Ray-paths for three 45° fan-beams, one passing through the insert, the other two just lying on either side of the insert. The plot is taken for circular Brass insert after 5 iterations.

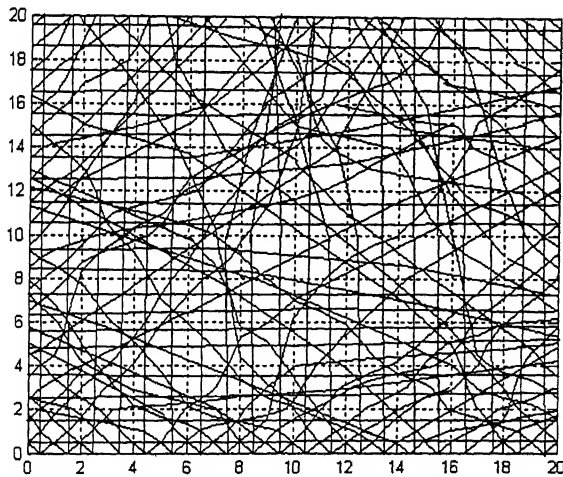


Figure 4.6 Typical ray-paths for circular Aluminium insert implanted in Steel for relaxation parameter = 0.1. The plot obtained is after 10 iterations.

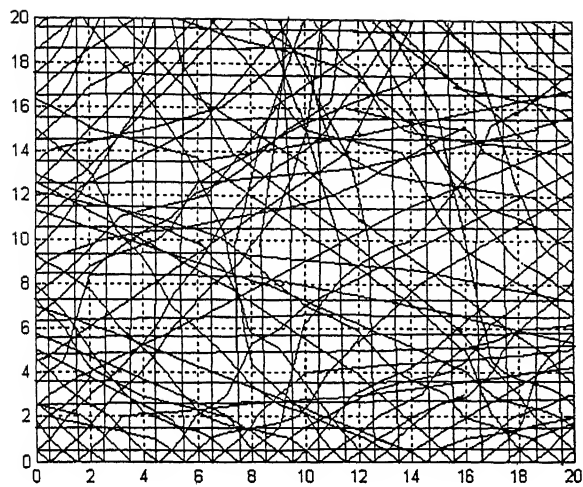


Figure 4.7 Typical ray-paths for circular Nickel insert implanted in Steel for relaxation parameter = 0.1. The plot is after 10 iterations.

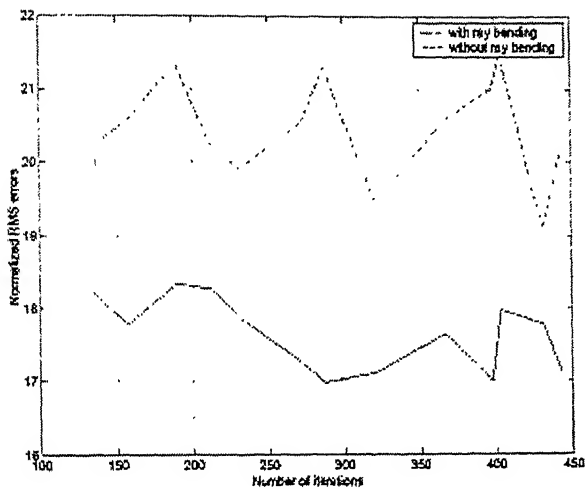


Figure 4.8 Plot of normalised RMS errors vs number of iterations with and without ray bending for circular Brass insert

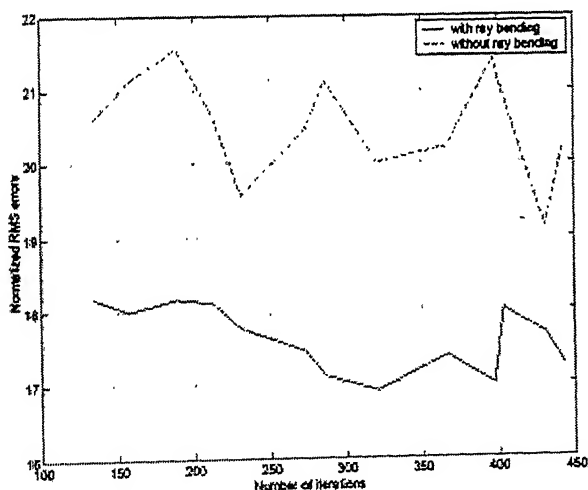


Figure 4.9 Plot of normalised RMS errors vs number of iterations with and without ray bending for elliptical Brass insert

Some images are shown below for the case of Brass insert in Steel where straight ray assumption has been taken. The images are shown for the purpose of comparison with images obtained using curved ray approach.

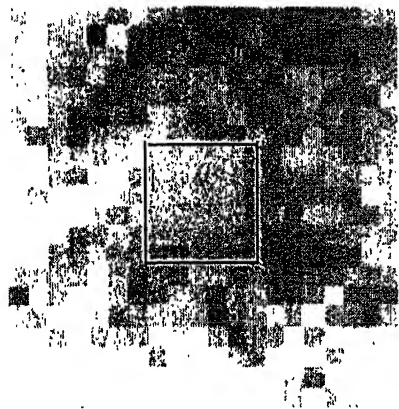


Figure 4.10 Tomographic reconstruction for square Brass Insert implanted in Steel with straight ray assumption for relaxation parameter = 0.1

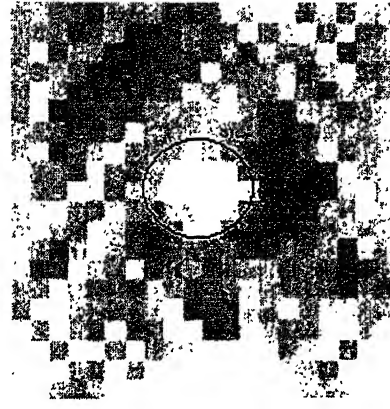


Figure 4.11 Tomographic reconstruction for circular Brass Insert implanted in Steel with straight ray assumption for relaxation parameter = 0.1

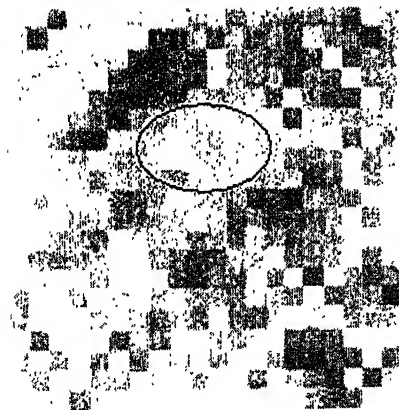


Figure 4.12 Tomographic reconstruction for elliptical Brass Insert with straight ray assumption for relaxation parameter = 0.1

The reconstructed images for the square shaped Aluminium insert implanted in Steel for four different relaxation parameters are given in figure 4.13-4.16.

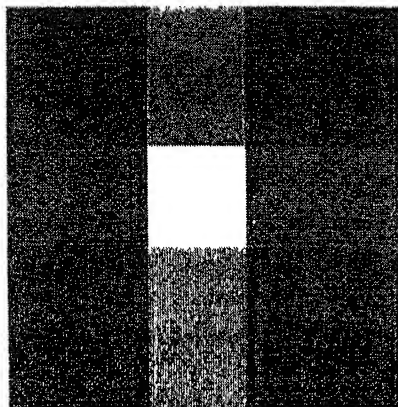


Figure 4.13 Tomographic reconstruction for square Aluminium insert implanted in Steel for relaxation parameter = 0.1

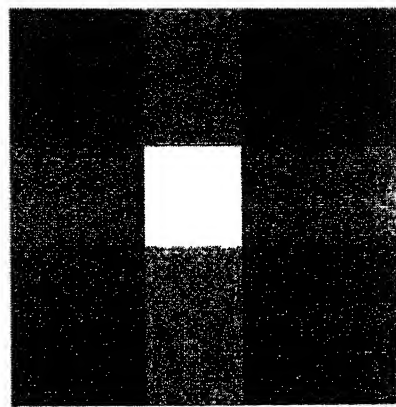


Figure 4.14 Tomographic reconstruction for square Aluminium insert implanted in Steel for relaxation parameter = 0.2

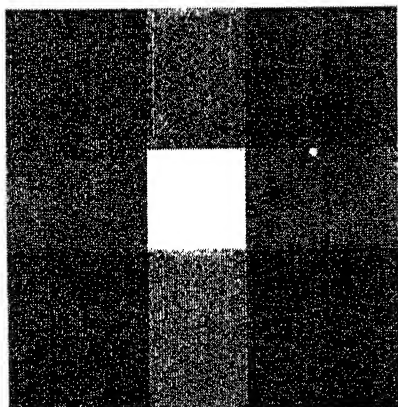


Figure 4.15 Tomographic reconstruction for square Aluminium insert implanted in Steel for relaxation parameter = 0.3

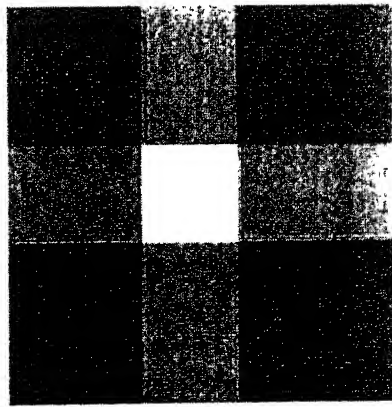


Figure 4.16 Tomographic reconstruction for square Aluminium insert implanted in Steel for relaxation parameter = 0.4

The reconstructed images for the circular shaped Aluminium insert implanted in Steel for four different relaxation parameters are given in figure 4.17 – 4.20.

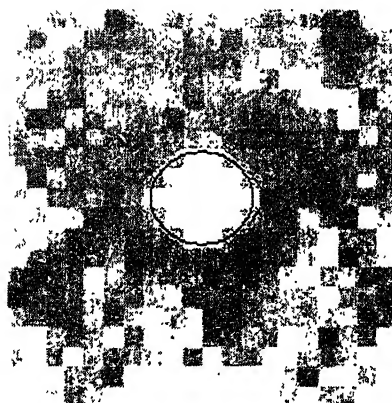


Figure 4.17 Tomographic reconstruction for circular Aluminium insert implanted in Steel for relaxation parameter = 0.1

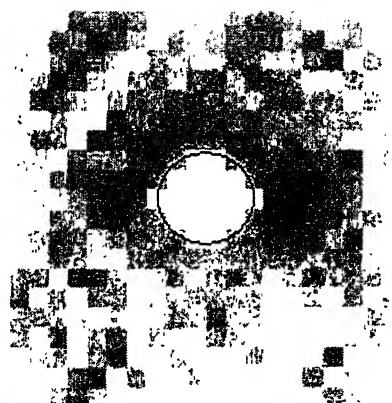


Figure 4.18 Tomographic reconstruction for circular Aluminium insert implanted in Steel for relaxation parameter = 0.2

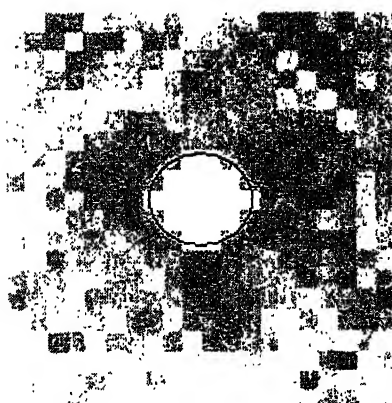


Figure 4.19 Tomographic reconstruction for circular Aluminium insert implanted in Steel for relaxation parameter = 0.3

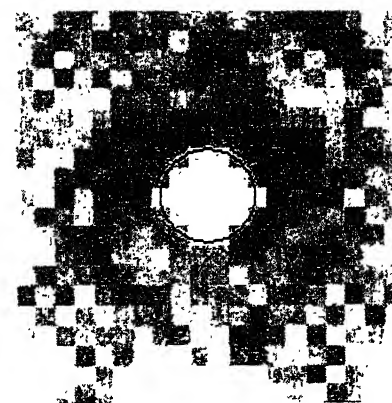


Figure 4.20 Tomographic reconstruction for circular Aluminium insert implanted in Steel for relaxation parameter = 0.4

The reconstructed images for the elliptical shaped Aluminium insert implanted in Steel for four different relaxation parameters are given in figure 4.21 – 4.24.

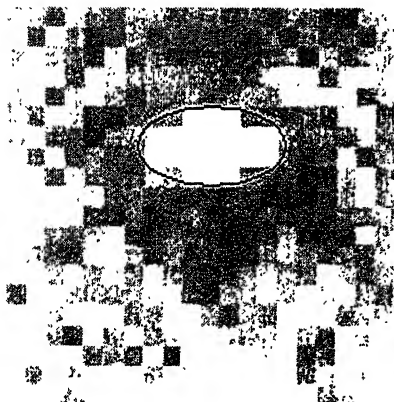


Figure 4.21 Tomographic reconstruction for elliptical Aluminium insert implanted in Steel for relaxation parameter = 0.1

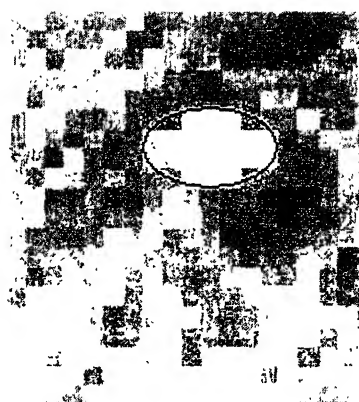


Figure 4.22 Tomographic reconstruction for elliptical Aluminium insert implanted in Steel for relaxation parameter = 0.2

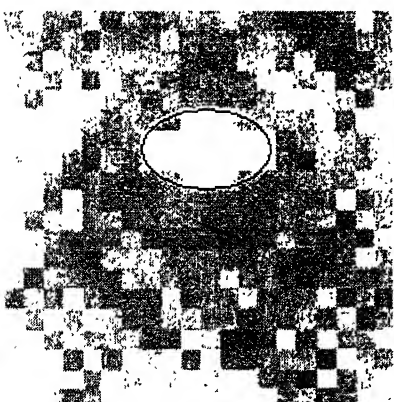


Figure 4.23 Tomographic reconstruction for elliptical Aluminium insert implanted in Steel for relaxation parameter = 0.3

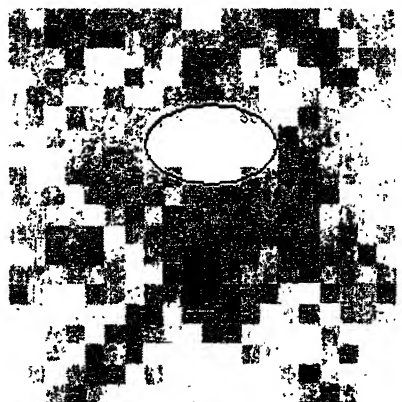


Figure 4.24 Tomographic reconstruction for elliptical Aluminium insert implanted in Steel for relaxation parameter = 0.4

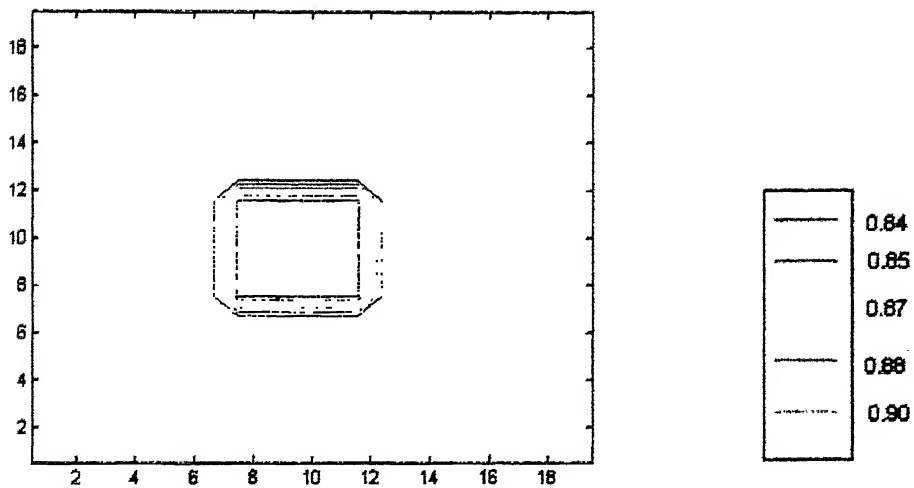


Figure 4.25 Contour plot for square Aluminium insert in Steel
The values in the legend are the normalized slowness values

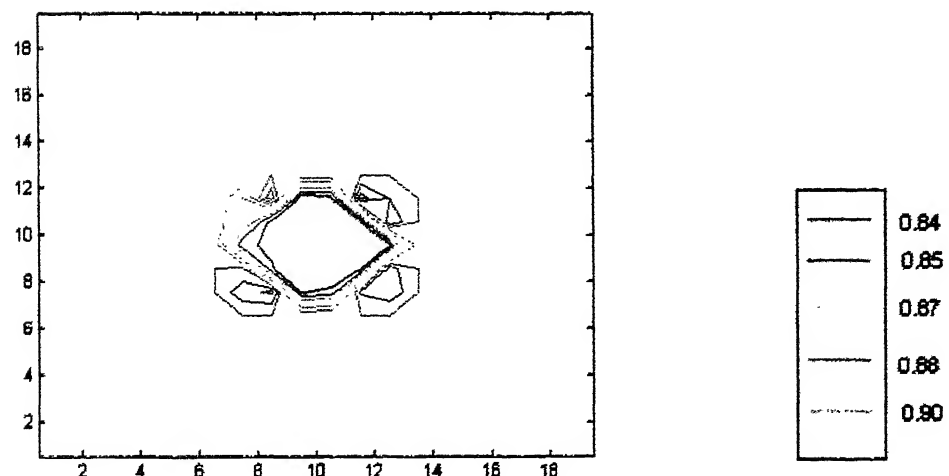


Figure 4.26 Contour plot for circular Aluminium insert in Steel
The values in the legend are the normalized slowness values

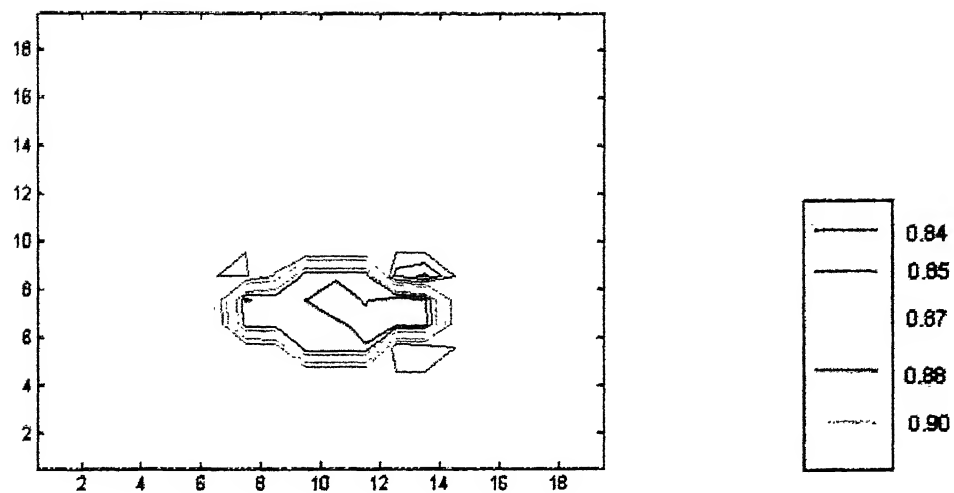


Figure 4.27 Contour plot for elliptical Aluminium insert in Steel
The values in the legend are the normalized slowness values

The reconstructed images for the square shaped Nickel insert implanted in Steel for four different relaxation parameters are given in figure 4.28 – 4.31.

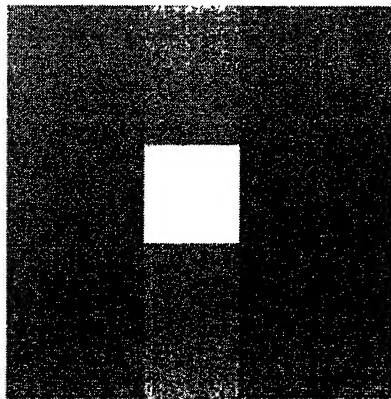


Figure 4.28 Tomographic reconstruction for square Nickel insert implanted in Steel for relaxation parameter = 0.1

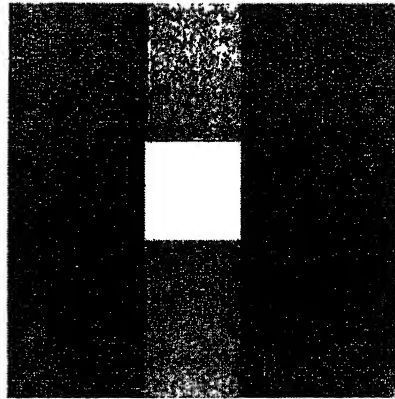


Figure 4.29 Tomographic reconstruction for square Nickel insert implanted in Steel for relaxation parameter = 0.2

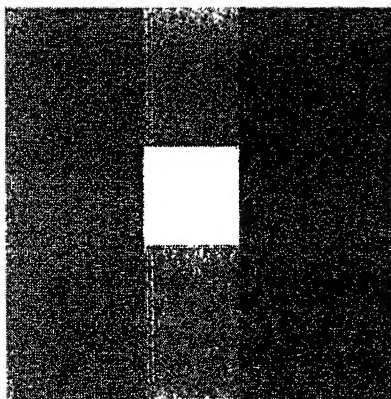


Figure 4.30 Tomographic reconstruction for square Nickel insert implanted in Steel for relaxation parameter = 0.3

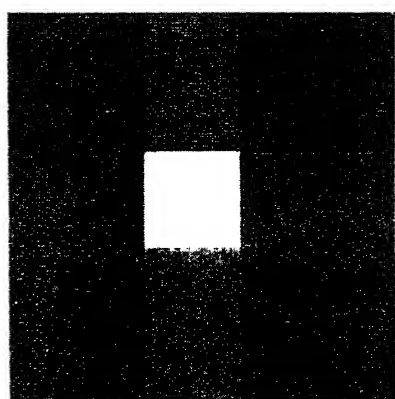


Figure 4.31 Tomographic reconstruction for square Nickel insert implanted in Steel for relaxation parameter = 0.4

The reconstructed images for the circular shaped Nickel insert implanted in Steel for four different relaxation parameters are given in figure 4.32 – 4.35.

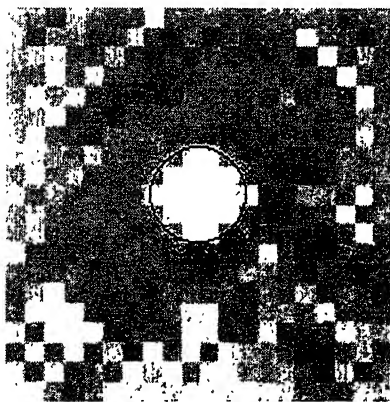


Figure 4.32 Tomographic reconstruction for circular Nickel insert implanted in Steel for relaxation parameter = 0.1

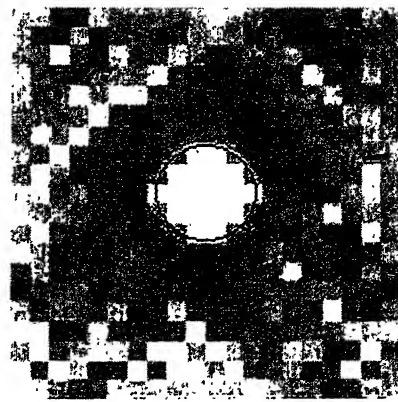


Figure 4.33 Tomographic reconstruction for circular Nickel insert implanted in Steel for relaxation parameter = 0.2

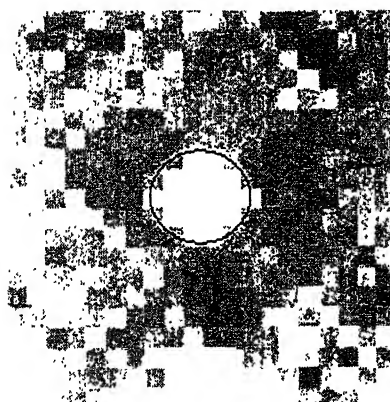


Figure 4.34 Tomographic reconstruction for circular Nickel insert implanted in Steel for relaxation parameter = 0.3

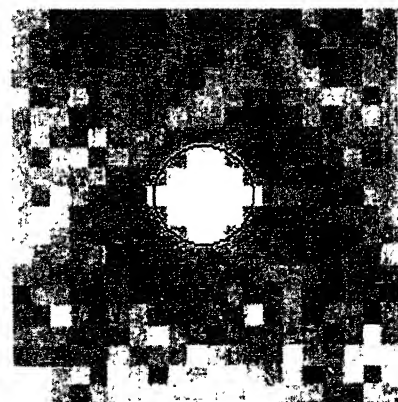


Figure 4.35 Tomographic reconstruction for circular Nickel insert implanted in Steel for relaxation parameter = 0.4

The reconstructed images for the elliptical shaped Nickel insert implanted in Steel for four different relaxation parameters are given in figure 4.36 – 4.39.

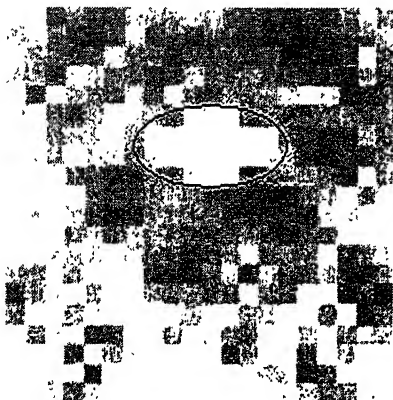


Figure 4.36 Tomographic reconstruction for elliptical Nickel insert implanted in Steel for relaxation parameter = 0.1

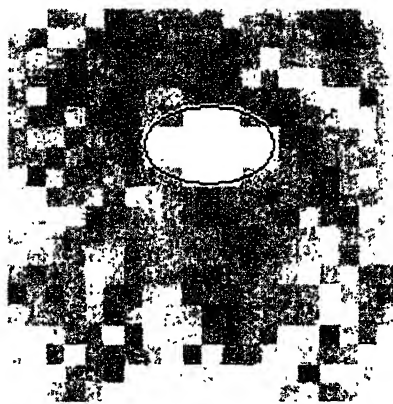


Figure 4.37 Tomographic reconstruction for elliptical Nickel insert implanted in Steel for relaxation parameter = 0.2

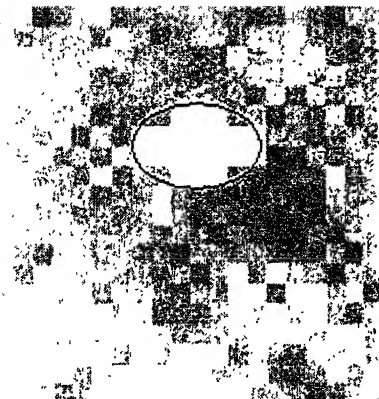


Figure 4.38 Tomographic reconstruction for elliptical Nickel insert implanted in Steel for relaxation parameter = 0.3

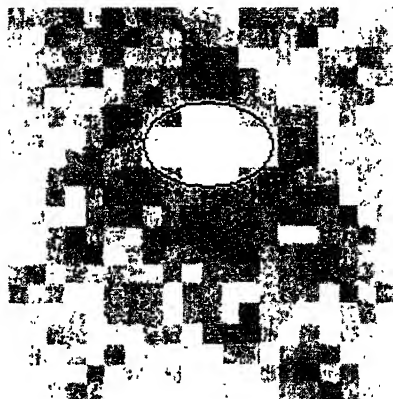


Figure 4.39 Tomographic reconstruction for elliptical Nickel insert implanted in Steel for relaxation parameter = 0.4

The reconstructed images for the square shaped Brass insert implanted in Steel for four different relaxation parameters are given in figure 4.40 – 4.43.

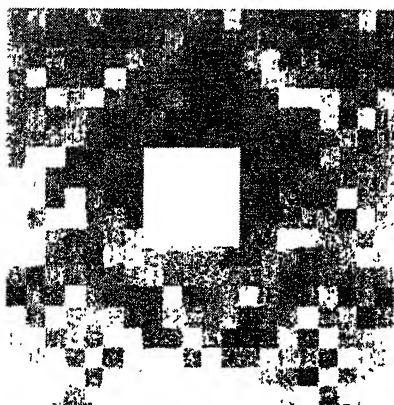


Figure 4.40 Tomographic reconstruction for square Brass insert implanted in Steel for relaxation parameter = 0.1

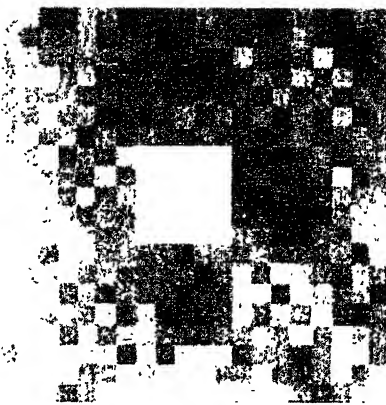


Figure 4.41 Tomographic reconstruction for square Brass insert implanted in Steel for relaxation parameter = 0.2

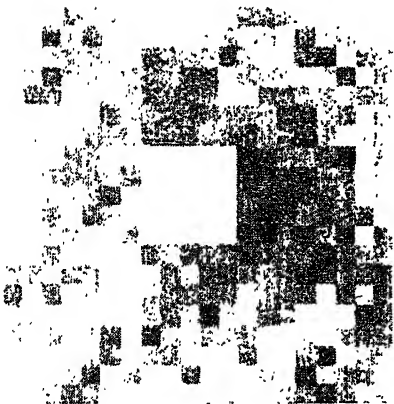


Figure 4.42 Tomographic reconstruction for square Brass insert implanted in Steel for relaxation parameter = 0.3

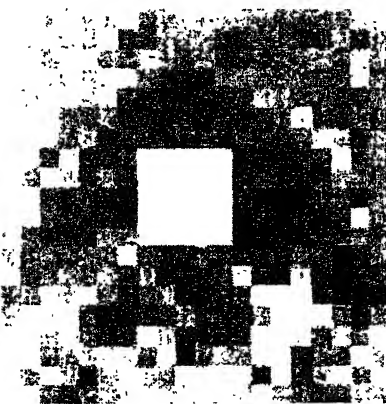


Figure 4.43 tomographic reconstruction for square Brass insert implanted in Steel for relaxation parameter = 0.4

The reconstructed images for the circular shaped Brass insert implanted in Steel for four different relaxation parameters are given in figure 4.44 – 4.47.

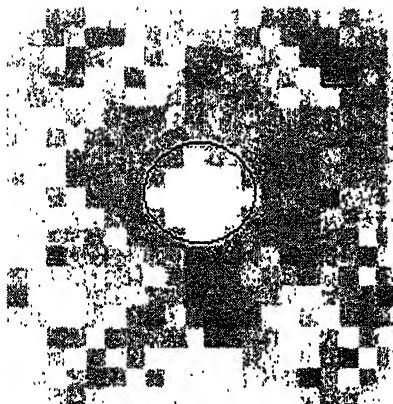


Figure 4.44 Tomographic reconstruction for circular Brass insert implanted in Steel for relaxation parameter = 0.1

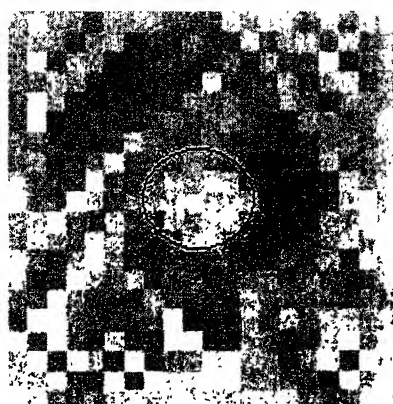


Figure 4.45 Tomographic reconstruction for circular Brass insert implanted in Steel for relaxation parameter = 0.2

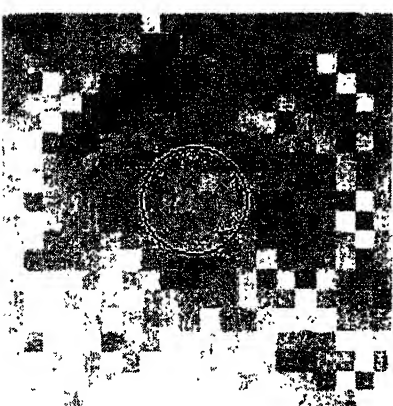


Figure 4.46 Tomographic reconstruction for circular Brass insert implanted in Steel for relaxation parameter = 0.3



Figure 4.47 Tomographic reconstruction for circular Brass insert implanted in Steel for relaxation parameter = 0.4

The reconstructed images for the elliptical shaped Brass insert implanted in Steel for four different relaxation parameters are given in figure 4.48 – 4.51.

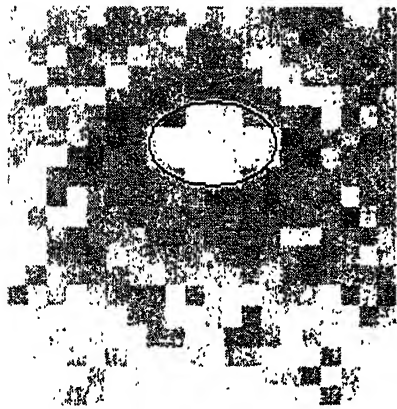


Figure 4.48 Tomographic reconstruction for elliptical Brass insert implanted in Steel for relaxation parameter = 0.1

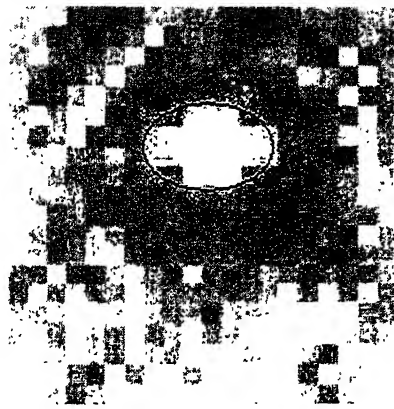


Figure 4.49 Tomographic reconstruction for elliptical Brass insert implanted in Steel for relaxation parameter = 0.2

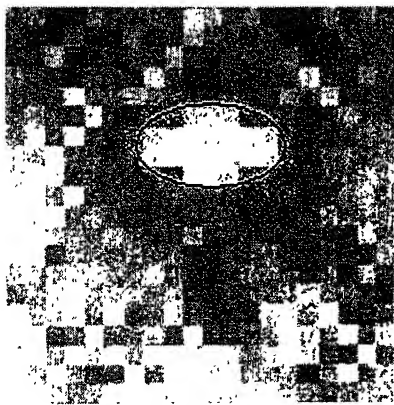


Figure 4.50 Tomographic reconstruction for elliptical Brass insert implanted in Steel for relaxation parameter = 0.3

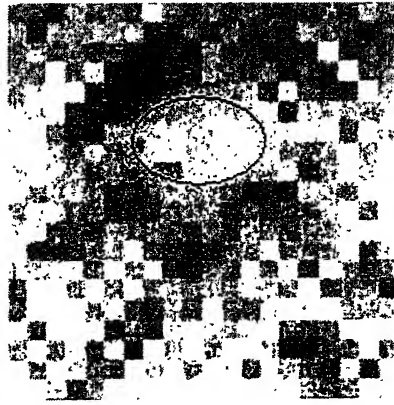


Figure 4.51 Tomographic reconstruction for elliptical Brass insert implanted in Steel for relaxation parameter = 0.4

4.6 Closure

Reconstructed images have been shown for all the three combinations of parent material and insert material. The quality of reconstruction is quite satisfactory for Steel-Aluminium pair and also for Steel-Nickel pair. However, it is not as good for Steel-Brass pair because of the larger velocity difference between Steel and Brass. The quality of reconstruction is also found to be best for relaxation parameters varying between 0.1 and 0.4. Hence all the images are shown for relaxation parameters lying within this range. Typical ray paths have been shown after the completion of a few iterations. Finally, a number of tables have been provided which furnish the variation in the RMS error as the relaxation parameter is varied. A table showing the comparison of the times taken for the algorithm to converge with and without ray bending has also been provided.

Chapter 5

Conclusion and scope of future work

5.1 Conclusion

In the present work, standard techniques have been applied for the tomographic reconstruction of samples with artificially implanted insertions. Based on the results obtained, the following inferences can be drawn:

- For isotropic materials the acoustic analogue of Snell's law is used to predict the path of the ultrasonic ray with reasonable accuracy in the presence of a refraction artifact.
- For tomographic reconstruction of circular and elliptical defects, recourse has been taken of standard edge detection techniques to find out correctly the interface for refraction. Without edge detection, the errors sometimes become unacceptably high.
- The normalized RMS error, which is a measure of the accuracy of reconstruction, is found to be consistently higher for images which have been reconstructed without using curved ray approach. The normalized RMS errors lie in the range of 21% for images obtained using straight ray approach and 18% for images obtained using curved ray approach.

References

1. Chen H.C, "Theory of Electromagnetic Waves-A coordinate free approach (*McGraw-Hill, New York, 1983*)
2. Synge, J. L, "Elastic waves in anisotropic media", *J. Math. and Phys.*, Vol.35, 1957, pp 323-334
3. Musgrave M.J.P, "Crystal Acoustics", *Holden Day*, 1970
4. Leander J.L, "On the relation between wavefront speed and the group velocity concept", *Journal of Acoustical society of America*, Vol. 100, No. 6, December 1996, pp 3503-3507
5. Crandall S.H, "On the use of Slowness diagrams to represent wave reflections", *Journal of Acoustical society of America*, Vol. 47, No. 5, 1970, pp 1338-1342
6. Fedorov F.I, "Theory of Elastic Waves in Crystals", *Plenum Press*, 1968
7. Auld B.A, "Acoustic Fields and Waves in Solids", Vols. I and II, *Wiley-Interscience*, 1973.
8. Henneke E.G, "Reflection – Refraction of a stress wave at a plane boundary between anisotropic media", *Journal of Acoustical society of America*, Vol. 51, No. 2, August 1972, pp 210-217
9. McNiven H.D, Mengi Y, " Critical angles associated with the reflection-refraction of elastic waves at an interface", *Journal of Acoustical society of America*, Vol. 44, No. 6, 1968, pp 1658-1663
10. Rokhlin S.I, Bolland T.K, Adler L, "Reflection and Refraction of elastic waves on a plane interface between two generally anisotropic media", *Journal of Acoustical society of America*, Vol. 79, No. 4, April 1986, pp 210-217
11. Harker A.H, Ogilvy J.A, " Coherent wave propagation in inhomogeneous materials: a comparison of theoretical models", *Ultrasonics*, Vol. 29, 1991, pp 235-243

12. Kak A.C., "Computerized Tomography with X-ray", *Proceedings of the IEEE*, Vol. 67, 1979, pp 1245-1275
13. Anderson A.H., Kak A.C., " Digital ray tracing in two-dimensional refractive index fields", *Journal of Acoustical society of America*, Vol. 72, 1982, pp 1593-1606
14. Bold G.E.J. and Birdsall T.G., " A top-down philosophy for accurate numerical ray tracing", *Journal of Acoustical society of America*, Vol. 80, 1986, pp 656-660
15. Wang Y.Q., and Kline R.A., "Ray tracing in isotropic materials: Application to tomographic image reconstruction", *Journal of Acoustical society of America*, Vol. 95, 1994, pp 2525-2532
16. Denis F. ,Basset O., Gimenez G., " Ultrasonic transmission tomography in refracting media: Reduction of refraction artifacts by curved-ray techniques", *IEEE transactions on Medical Imaging*, Vol.14, 1995, pp 173-188